Chemistry and Physics of Lipids 276–277 (2026) 105577

Contents lists available at ScienceDirect

Chemistry and Physics of Lipids

journal homepage: www.elsevier.com/locate/chemphyslip

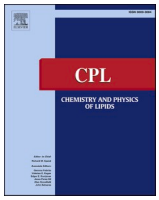

Review of lipid bilayer structure

John F. Nagle

Department of Physics, Carnegie Mellon University, Pittsburgh, PA 15213, USA

ARTICLE INFO

Keywords:
Lipid bilayers
X-ray scattering
Neutron scattering
Form factors
Gel phase
Fluid phase
Ripple phase

ABSTRACT

The structure of well-hydrated, single-component, lipid bilayers is reviewed. Definitions are provided for the parameters that describe structure at various levels of refinement. Comparisons in the structure are made for lipids with different head groups and hydrocarbon chains. Experimental methods include x-ray scattering, neutron scattering, NMR, and densimetry. Interpretation of the scattering experiments is reviewed in some detail and critically examined. Comparison is made to structural parameters obtained from simulations. Chain disordered fluid phase structure is compared to chain ordered gel phase structure, and other chain ordered structures are also briefly reviewed. Even for these simple lipid bilayers, some structural aspects remain unresolved and await further research.

1. Introduction

Studies of the structure of lipid bilayers have been going on for more than half a century, motivated by their relevance to biomembranes. However, there are aspects of lipid bilayers that are more concerned with their physics and chemistry, and that is the focus of this review. In particular, while biomembrane studies are understandably focused on the fluid bilayer phases that are most biologically relevant, this review also encompasses phases that occur at lower temperatures. This is essentially an update of an earlier review (Nagle and Tristram-Nagle, 2000) to take account of much that has since transpired. Better values of structural parameters have been obtained due to improved methods, and more lipid bilayers have been studied. Nevertheless, it is pointed out that there are still interesting, unresolved issues even in this much-studied field. This review does not attempt to discuss all the papers in this much-studied field. Instead, it is focused on critical, in-depth discussion of those that I think are most important methodologically.

At the outset, let us remind ourselves that atomic-level crystallographic structure does not exist for the most biologically relevant fully hydrated fluid phases. This is not surprising. Water substantially alters the balance of interaction energies between lipids compared to the nearly dry crystalline state, thereby allowing for substantial fluctuations and disorder, even when bilayers are in multilamellar arrays and even for the relatively ordered gel and subgel bilayer phases. The substantial effect of hydration on bilayer structure has been thoroughly reviewed (Nagle and Tristram-Nagle, 2000; Rand and Parsegian, 1989) and subsequent studies have usually been done under full hydration, in contrast to notable earlier studies that were done under 66% relative humidity (Wiener and White, 1991) which removes most of the water, so fully hydrated bilayers are the focus of this review. Thus, it makes little sense to contemplate an atomic level structure, and its absence should not be blamed on poor diffraction technique or sample preparation; rather, such structures simply do not exist.

Nevertheless, there is average structure that is subject to thermally induced disorder with root mean square deviations that are substantially larger than atomic sizes. Then, the appropriate description of structure is that of statistical distribution functions, which are spatially broader than atoms. Even though experimental determination of distribution functions for individual atoms is usually not feasible, it is feasible to consider distribution functions for aggregates of atoms within the lipid molecule, which we here call moieties. An example of a moiety is the entire headgroup, where 'headgroup' is a conventional term for the hydrophilic part of a lipid molecule. A smaller moiety is just a phosphate. It is unfortunate that these pieces of lipids are often called components in the literature, including in my own papers. Here, the pieces of lipids are called moieties, and components have the more conventional meaning of different lipids in mixtures. Although most current research deals with lipid bilayers with many components, this review is limited to lipid bilayers with a single component in order to focus on the best determined structure and the methodologies for obtaining it.

This review begins with a section that elucidates many of the structural quantities of interest, and it provides a tabulation of some of the basic results from the literature. There are then two main sections that go into much more detail, including critical reviews of some of the methodologies employed. Section 3 reviews the fluid (F) phase and Section 4 reviews the gel (G) phase, often called the L_β phase. The F

E-mail address: nagle@cmu.edu.

https://doi.org/10.1016/j.chemphyslip.2026.105577
Received 22 October 2025; Received in revised form 4 March 2026; Accepted 25 March 2026
Available online 31 March 2026

phase is often called the L_d or the L_α phase. It is also often called the liquid crystalline phase, although this conflicts with the liquid crystal literature in which the multilayered G phase is also a liquid crystal. Subsections of these major sections delve deeper into the methodology. The methodology is sufficiently different for the F and G phases that they are best treated in separate sections. In particular, simulations are now playing a large role for fluid phase structure, as described in Section 3.4, where very detailed results are provided for the DOPC bilayer. A relatively minor Section 5 reviews ripple and subgel liquid crystal phases.

2. Overview of some average structural quantities

This section focuses on average quantities and leaves the spatial distributions for later. Fig. 1 illustrates some of the most important quantities. The sketch on the left represents an average lipid molecule taken from one monolayer of a bilayer. This lipid, labelled (A), has an area/lipid $A_L = 45$ Å^2. Neighboring lipids in this bilayer are not shown as they have the same average dimensions, and they are supposed to be packed together so that there are no gaps for water in the hydrocarbon chain region. For comparison, the sketch on the right represents an average lipid (B) in a different bilayer that has an area/lipid $A_L = 75$ Å^2. Note that the large difference in A_L is meant to illustrate some subsequent points regarding how structural parameters depend upon the area and not to represent gel versus fluid phase lipids. Accordingly, both these lipids have the same volume $V_C = 900$ Å^3 of the chain region, and the same headgroup volume $V_H = 300$ Å^3, and the same total volume/lipid $V_L = V_C + V_H = 1200$ Å^3. The headgroups are drawn with rather simple shapes that are assumed to be the same for both lipids. Each bilayer has several different thicknesses of interest. The steric thickness D_S is defined to include all but a negligible fraction of protruding outlier atoms so that there would be a large hard-core repulsive force between two identical bilayers whose centers come closer together than D_S. The hydrocarbon thickness $2D_C$ is defined to include only the tails from the lipids in both monolayers, each monolayer having an average thickness of D_C in symmetric bilayers. V_L and A_L lead to the so-called Luzzati thickness D_B, which is defined as

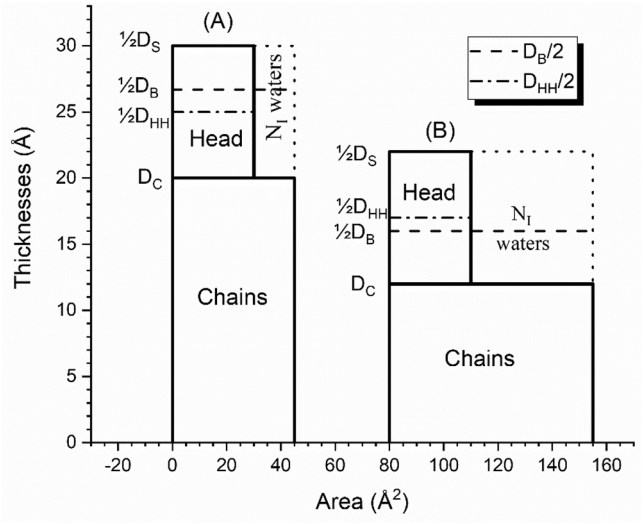

Fig. 1. A cartoon for the average structure of a lipid taken from the upper monolayer of a single-component symmetric bilayer. On the left, the lipid is taken from a bilayer that has small area per lipid A_L and on the right, the same lipid is taken from a bilayer that has large A_L. Neighboring lipids (not shown) are packed together so that water is excluded from the chain regions. The region next to each headgroup contains N_I interfacial water molecules. The sizes of the labelled regions (the product of the distances along the x and y axes) give the head and chain volumes, each of which is drawn to be equal for the two lipids.

$$D_B = 2V_L/A_L. \quad (1)$$

D_B can be thought of as rearranging the lipid volumes into a single slab that contains no water and a single slab of water that contains no lipid, thereby conceptually eliminating the interfacial headgroup region between the hydrocarbon thickness and the steric thickness. D_B is essentially the distance between the two Gibbs surfaces that represent the interfaces between lipid and water. Furthermore, the thickness D_{HH} is defined as the distance between the peaks in the electron density profile of the opposite monolayers; this is related to the distance D_{PP} between the phosphates on opposite monolayers. For isotropic multilamellar vesicles (MLV) and oriented stacks of bilayers, there is the repeat spacing D, which includes a total of N_W water molecules per lipid, typically exceeding 20 for fully hydrated fluid phase phosphatidylcholine (PC) lipids. The smaller number of those waters located just in the interfacial region illustrated by the dotted boxes in Fig. 1 is designated N_I; $N_I = 5$ in the lipid on the left side of Fig. 1 and 15 in the lipid on the right-hand side. Structure also includes the orientational order parameters S_{CD} for the hydrocarbon tails and the tilt angle θ_H of the headgroup relative to the bilayer normal. The gel phase introduces the tilt angle θ_t of the hydrocarbon tails, and the ripple phase introduces a ripple wavelength λ_r. Other structural quantities will be introduced as we go along.

Interest in these quantities is evidenced by many papers since the 1970s written by prominent research groups. Many values have been produced in highly cited papers, but there was considerable disagreement between the early values. For example, the values of A_L for fluid phase DPPC spanned the range from 56 Å^2 to 72 Å^2 as compiled in the 2000 review (Nagle and Tristram-Nagle, 2000). This current review does not repeat critiques of the earlier work but focuses on the current status.

Table 1 collects results for four of the most important average quantities: the volume per lipid V_L, the area per lipid A_L, the head-head thickness D_{HH}, and the hydrocarbon thickness $2D_C$. The thermodynamic phase clearly matters for structure, as can be seen by comparing the four lipids for which both gel and fluid results are shown. Compared to gel phase bilayers, the fluid phase has considerably larger V_L and A_L and smaller thicknesses, even if one were to adjust for temperature differences.

Comparing the fluid phase bilayers, it is not surprising that thickness generally increases with increasing numbers of carbons N_C on the chains. A striking exception in this table is DPhyPC, which has four branched methylenes on each chain, thereby increasing the chain width relative to the linear hydrocarbon chains of the other lipids, and this increases A_L substantially.

The degree of unsaturation of the hydrocarbon chains matters. Having more double bonds N_{db} with the same N_C tends to reduce the hydrocarbon thickness D_C and increase the area A_L. For example, although DOPC has four more carbons than DPPC, its D_C at 30°C is the same as that of DPPC at 50°C, even though the higher temperature of DPPC also reduces thickness. Because the thicknesses are nearly equal, the larger volume of DOPC requires a larger area than that of DPPC. Lipids with mixed chains like POPC have intermediate values of structural parameters between those of the corresponding same-chain lipids, such as DPPC and DOPC.

Headgroups also affect the structure, with PE lipids having the smallest areas and PG lipids the largest. The ether-linked backbone in DHPC appears to make its area somewhat larger than that of ester-linked DPPC, and the sphingomyelin link in palmitoyl sphingomyelin (PSM) makes its area somewhat smaller. Varying the relative chain lengths of saturated chains makes little difference to the structural quantities as shown in the last three rows of Table 1; however, as one would expect, the distribution of the terminal methyl ends of the hydrocarbon chains varies (Frewein et al., 2021).

A central structural ingredient in Table 1, the volume per lipid V_L, is the most accurate of all structural quantities, with uncertainties sometimes less than 1 Å^3. Of course, V_L is generally larger for lipids with

Table 1
Selected structural results for lipid bilayers in the fluid F and gel G phases. N_C is the number of carbons on both hydrocarbon chains and N_{db} is the number of double bonds.

Lipid	N_C	N_{db}	T (°C)	ϕ	V_L (Å^3)	A_L (Å^2)	D_{HH} (Å)	$2D_C$ (Å)
DPPC (Nagle et al., 2019a)	32	0	20	G	1144	47	45	34
DPPC (Kucerka et al., 2011)	32	0	50	F	1229	63	39	29
DMPC (Tristram-Nagle et al., 2002)	28	0	10	G	1041	47	40	30
DMPC (Kucerka et al., 2011)	28	0	30	F	1100	60	35	26
DLPC (Kucerka et al., 2011)	24	0	30	F	991	61	30	22
DOPC (Braun et al., 2013)	36	2	30	F	1303	67	37	29
DEPC (Nagle et al., 2023)	44	2	10	G	1307	48	54	42
DEPC (Kucerka et al., 2009)	44	2	30	F	1524	66	45	36
POPC (Kucerka et al., 2011)	34	1	30	F	1256	64	37	29
SOPC (Kucerka et al., 2011)	36	1	30	F	1309	66	39	30
PDPC (Marquardt et al., 2020)	38	6	30	F	1306	71	33	28
DPhyPC (Kucerka et al., 2011)	40	0	30	F	1427	81	35	27
DLPE (McIntosh et al., 1986)	24	0	20	G	833	41	37	27
DLPE (Kucerka et al., 2015a)	24	0	35	F	901	52	33	25
POPE (Kucerka et al., 2015a)	34	1	35	F	1175	58	38	32
SOPE (Kucerka et al., 2015a)	36	1	35	F	1230	57	42	34
POPS (Pan et al., 2014)	34	1	25	F	1199	62	42	29
DOPS (Petrache et al., 2004)	36	2	30	F	1228	65	38	30
DOPG (Pan et al., 2012a)	36	2	30	F	1265	71	36	28
DHPC (Pan et al., 2012b)	32	0	60	F	1239	67	38	27
PSM (Doktorova et al., 2020)	28	0	45	F	1152	60	39	29
MSPC (Frewein et al., 2021)	28	0	50	F	1232	62	36	29
SMPC (Frewein et al., 2021)	28	0	50	F	1232	62	35	29
PMPC (Frewein et al., 2021)	26	0	50	F	1176	63	34	27

longer hydrocarbon chains. The more significant difference is between gel and fluid phases, as shown for DPPC, DMPC and DLPE in Table 1. However, it may be noted that all experimental methods assume that all the water in the system, including that in the interfacial region, has the same volume as bulk water, so any difference in the volume of water interacting strongly in the interfacial region is necessarily assigned to the lipid. A recent analysis allowed for a different density of water in the headgroup region, but then using the measured volume is inconsistent; however, the suggested 3% denser headgroup water had a negligible effect on the results in Table 1 (Frewein et al., 2021). Earlier results from the Pabst group were also found to be in close agreement with other lipids in Table 1 (Heftberger et al., 2014; Ollila and Pabst, 2016). An analysis of simulations also found little difference in water volume in the headgroup region versus the pure water region (Nagle et al., 2019b).

The reader may notice that no uncertainties are given in Table 1, although the original papers usually quote uncertainties. That is because those uncertainties are overridden by methodological uncertainties that are examined in the subsequent sections. However, those uncertainties are unlikely to affect the differences between lipids that have been addressed in this section.

3. Fluid phase structure

We now go into considerable more depth for the structure of the F phase. This main section overviews some results in the context of the quantities described in Section 2 and then shows the kind of scattering data used to model the structure. Subsection 3.1 delves deeper into how that modelling is performed, followed by subsection 3.2 that shows the specific example of DOPC. Subsection 3.3 briefly recalls classical work on specifically deuterated lipids and relates those results to more recent results. Subsection 3.4 compares simulation results with scattering results, and it contains the most up-to-date detailed structure of DOPC.

For lipid bilayers with a single component the references in Table 1 are replete with graphs showing how the structural quantities depend upon chain length and temperature. Here, I choose a different way to view the structure that retains that information but that better focuses on the interfacial region. I do this by looking at differences in two thicknesses as a function of the area as illustrated in Fig. 2. Why this is interesting is illustrated using the cartoon of the interfacial region in Fig. 1. The headgroups in the cartoon are simple rectangles such that the local headgroup area is the same at different z levels, but this particular shape is not important. Any shape obeys a simple relation,

$$D_B/2 - D_C = V_H / A_L, \tag{2}$$

where V_H is the volume of the headgroup, so the distance between the Gibbs dividing surface ($D_B/2$) and the top of the hydrocarbon region (D_C) should decrease as the area A_L increases if the well solvated headgroup volume V_H doesn't change.

Fig. 2 shows $D_B/2 - D_C$ vs. A_L with a constant V_H for the results from a study of many PG lipids at several temperatures (Pan et al., 2012a). Other important literature conclusions can also be drawn from Fig. 2, such as the unsurprising increase in A_L with increasing T and the generally larger A_L for more double bonds. However, the T dependence is stronger for DLPG, resulting in a slightly larger A_L (71.5 Å^2) at the highest T (60°C) than for the mixed chain lipids SOPG and POPG. The effect of the second double bond in DOPG is especially strong, evident by comparing saturated, singly unsaturated and di-unsaturated PGs. This differs for PC lipids, where the greatest increase in A_L occurs upon

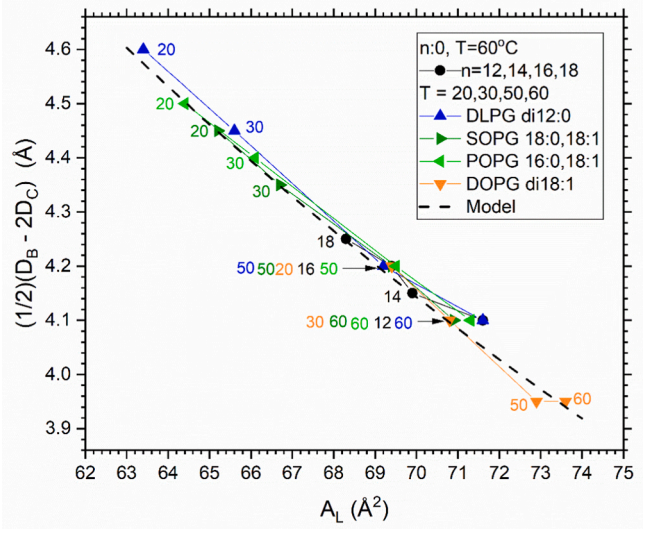

Fig. 2. A new way to examine the interface. Numbers next to triangular symbols are temperatures. Numbers n = 12–18 next to circular symbols give chain lengths of saturated lipids (n:0), and these data are at 60 °C. Data are from (Pan et al., 2012a). DLPG at 60 °C has two superimposed symbols. Headgroup V_H is 291 Å^3.

adding the first double bond (Kucerka et al., 2015b). Like the PC lipids, A_L decreases with increasing chain length at the same T.

It is also desirable to break down the total volume of a lipid molecule into the volumes of its moieties. The first such division separates V_L into the headgroup volume V_H and the chain volume V_C. The chain moiety includes the hydrocarbon tails from the terminal methyls to the first methylene (the second fatty acid carbon), while the carbonyl glycerol (CG) linkage is included with the headgroup. Table 2 shows results for V_H that are roughly the same for lipids with the PC headgroup and smaller for the PG, PE and PS headgroups. Table 2 also shows the average volume V_{CH2} of the methylenes on the hydrocarbon chains. As one would expect, V_{CH2} is smaller for gel phases, as shown for DPPC and DLPE. Comparing the fluid phases and noting temperature differences, V_{CH2} tends to be larger for lipids with double bonds and also for charged headgroups (PG and PS) than for saturated PC lipids.

A time-honored method to obtain V_{CH2} measures the volumes of homologous lipids that differ only in the number of chain methylenes. Then, V_{CH2} is the volume difference divided by the difference in numbers of methylenes. This is basically the assumption that V_L can be obtained by adding a temperature-dependent set of moiety volumes, and it has been shown that this linear additive model reproduces measured V_L quite well for different lipid classes (Koenig and Gawrisch, 2005; Uhrikova et al., 2007). Recently, we noticed an anomaly in the temperature dependence of V_H that led to a re-examination of moiety volumes. With the insight obtained from simulations, we devised a procedure to further refine moiety volumes (Nagle et al., 2019b). The entries for fluid phase DPPC and DOPC in Table 2 are from this re-examination.

For convenience, Table 2 also shows results for gel phase moieties that are obtained from a different method, as will be discussed further in Section 4. Since the headgroup is well solvated in both the gel and fluid phases, I have often assumed that V_H is the same in both phases. This assumption is supported by the overlap of this range with the range of other PC fluid phase values of V_H shown in Table 2 that were obtained by the preceding method (Nagle et al., 2019b). On the other hand, it has been concerning that considerably higher values of V_H for PC monolayers have been recently reported (Harvey et al., 2023). This and further partitioning of V_H and of V_C into the volumes of even smaller moieties will be taken up subsequently.

The V_H values in Table 2 for DOPS, DOPG and DLPE were obtained by assuming that V_C was the same as for the PC lipid with the same chains at the same temperature. Thus there is a slightly temperature dependent value of V_H because the coefficient of expansion V_L is slightly different for different lipids, but that difference is typically less than 5 Å^3, so a single value is generally used. This gives V_C from which V_{CH2} is calculated using the ratios of the methine and terminal methyl volume to the methylene volumes which are obtained by the modelling of low angle x-ray scattering and from simulations. Since those ratios are very similar for all the lipids, this means that the agreement of V_{CH2} for lipids with other headgroups is necessarily similar to those of the PC lipids with the same chains. Since there are a number of assumptions here, it might be interesting to obtain gel phase data for these other headgroups.

The fluid phase structural results in Table 1 come from studies of two types of fully hydrated bilayers. Extruded unilamellar vesicles (ULVs) with 30 nm radii have provided continuous form factors. X-ray scattering obtains $F_e(q_z)$, which is the Fourier transform of the electron density profile $\rho_e(z)$ along the bilayer normal, and neutron scattering obtains $F_n(q_z)$, which is the Fourier transform of the neutron scattering length density profile $\rho_n(z)$. X-ray scattering from multilamellar stacks of bilayers also provides $F_e(q_z)$ by analysis of diffuse scattering. (There are also pseudo-Bragg peaks, but for the fluid phase unlike the gel phase there is more information in the diffuse scattering than in these peaks.) Analysis of multilamellar stack data separates the scattering intensity into the non-Bragg so-called structure or interference factor S(q) due to bilayer undulations and the so-called form factor $F(q_z)$ along the sample normal. However, because of undulations, $F(q_z)$ averages over a distribution of slightly tilted projections of flat bilayers, as previously emphasized (Nagle and Tristram-Nagle, 2000). To obtain $F(q_z)$ for flat bilayers, it suffices to scale the q_z axis to $(1+\delta_{uc})q$, where δ_{uc} depends upon the bending modulus and is about 0.02 for DOPC. In principle, an undulational correction factor should also be applied to the ULV form factor. Appendix E in (Jablin, 2015)) derives that δ_{uc} should be at least a factor of 2 smaller for vesicles, and would be even smaller if the vesicles have a small effective surface tension. In any case, agreement of $F_e(q_z)$ in overlapping regions of q_z provides assurance that the strong curvature of unilamellar vesicles and the lack of an undulational correction factor either aren't important or cancel each other out.

While real-space structure is the ultimate goal, it is important to emphasize that it is the form factors that are the data closest to the experiments. Figs. 3 and 4 show form factor data for the DOPC bilayer. The multilamellar oriented (ORI) stack X-ray data consist of an average of many data sets taken by my group over multiple years. They extend to higher q_z than the unilamellar (ULV) data, but the latter go to smaller values of q_z, so combining them provides a larger q_z range. Neutron scattering has only been obtained for ULV samples, but at several D_2O concentrations to provide additional contrast $\rho_n(z) - \rho_{nw}$ with water ρ_{nw}. The neutron form factors have considerably different q_z dependence than x-ray form factors as can be seen by comparing Fig. 4 with Fig. 3. For x-ray scattering the largest real space contrast $\rho_e(z) - \rho_{ew}$ with the electron density of water ρ_{ew} is located in the electron dense headgroup region, especially due to the phosphorus atom. This makes x-ray data most sensitive to the D_{HH} parameter. For neutrons with deuterated water the contrast $\rho_n(z) - \rho_{nw}$ is roughly constant throughout the thickness of the bilayer, and this makes neutron data most sensitive to the D_B

Table 2
Some volumetric results.

	T	V_L	V_H	V_{CH2}
lipid	°C	Å^3		
DPPC (Nagle et al., 2019b)	20	1144	331	25.3
DPPC (Nagle et al., 2019b)	50	1232	328	28.0
DOPC (Nagle et al., 2019b)	40	1312	320	28.3
DHPC (Pan et al., 2012b)	60	1239	326	28.2
DOPG (Pan et al., 2012a)	50	1281	291	28.7
DLPE (McIntosh et al., 1986, Wiener et al., 1988)	20	863	252	25.5
DLPE (Kucerka et al., 2015a)	55	919	245	28.1
DOPS (Petrache et al., 2004)	30	1228	244	28.3

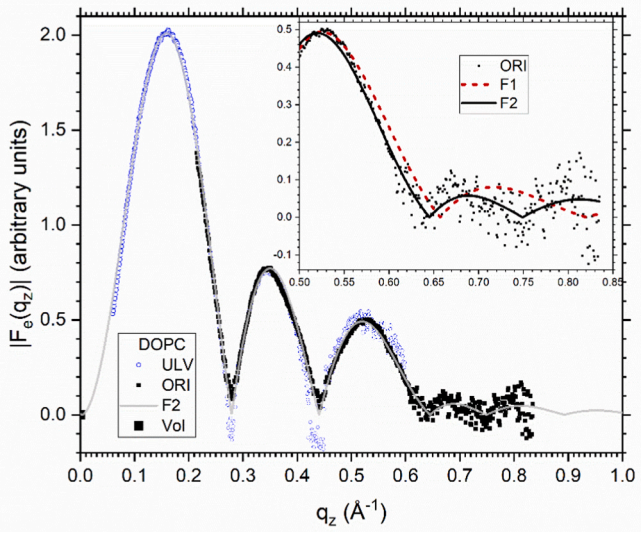

Fig. 3. X-ray form factors for DOPC from oriented samples (ORI, solid circles) and from unilamellar vesicles (ULV, open circles). These data are available in Supplementary Material. The square very near the origin comes from Eq. (3). The F1 and F2 fits to the data are described in subsection 3.2.

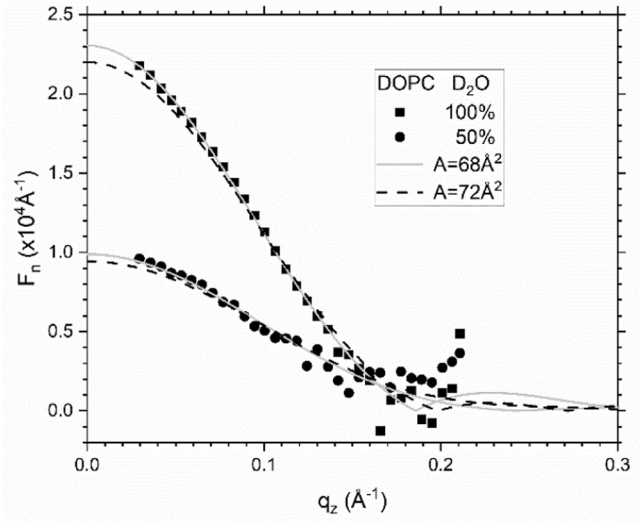

Fig. 4. Neutron form factors from ULV samples with two heavy water concentrations (Kucerka et al., 2009). Two fits to the data are described in subsection 3.2.

parameter in Fig. 1.

3.1. *Extracting structure from scattering form factors - modeling*

The nearly continuous form factors raise the possibility of obtaining $\rho_e(z)$ and $\rho_n(z)$ profiles by Fourier transform, but there are usually missing data for small q_z in the x-ray data (with a recent exception (Frewein et al., 2021)), and the neutron data do not extend very far in q_z. Another problem with this approach is that form factors generally have an unknown experimental multiplicative factor. One can obtain this factor to within the uncertainty in A_L by extrapolating the data to q= 0 and applying (Nagle and Wiener, 1989)

$$A_L F(0) = 2(n_L^* - V_L \rho_W^*), \tag{3}$$

where n_L^* is the number of electrons or total neutron scattering length of the lipid, and ρ_W^* is the electron density or neutron scattering length density of water. While this is an important relation, $F_x(0)$ may be too small for x-ray scattering to obtain a reliable scale factor, as is the case for DOPC, where F(0) is essentially zero to high accuracy since V_L is highly accurate.

In my opinion the best method to obtain structural quantities of interest devises a plausible model for ρ(z) that involves a set of adjustable parameters P from which model form factors $F(q_z)$ can be calculated for any q_z value for any real space property ρ(z)

$$F(q_z) = \int dz(\rho(z) - \rho_W)\cos(zq_z). \tag{4}$$

Many models have been employed over the years that were deficient because their associated volumes violated the physical constraint that the volume between z and z + dz has to be constant as a function of z (Wiener and White, 1991; Wiener et al., 1989; Klauda et al., 2006). Two more recent models conserve volume (Kucerka et al., 2008; Shekhar et al., 2011). Each moiety m is represented by a volume probability distribution function $v_m(z)$ which directly gives $\rho_e(z)$ and $\rho_n(z)$ and hence $F_e(q_z)$ and $F_n(q_z)$ via Eq. (4). Smooth analytic functions can be chosen for all but one of the moieties, but to conserve volume the last moiety (water is best) is constrained by the sum of all the $v_m(z)$ adding to one at all z. It is important that care be taken when parsing the lipid into moieties. In particular, the conventionally defined phosphocholine (PC) moiety is spatially inhomogeneous with respect to neutron scattering lengths. The hydrogens on the choline methyls have strongly negative contrast with deuterated water, whereas the other PC atoms have small contrast, so for neutron scattering data, it is best to parse the PC headgroup into a three methyl moiety and a moiety with the remaining PC atoms. This parsing, called the SDP model (Kucerka et al., 2008), was used since 2008 for the fluid phase results in Table 1. (Note, however, that the SDP software that runs the fitting allows any parsing of the lipid molecule, including the conventional parsing which is often appropriate for fitting X-ray data alone.) The hydrocarbon region, which is defined to include methylenes, terminal methyls, and double-bonded methines on the hydrocarbon tails, is represented by a pair of error functions $v_{HC}(z)$ that has a width and a parameter to taper the edges at the interface with the headgroups with a plateau value fixed at 1 to exclude water from the central constant part of the hydrocarbon region. (Note that less than 0.1% water suffices to account for water permeability.) Pairs of error functions can also be used for all the moieties (Shekhar et al., 2011), while the SDP model uses Gaussians for the headgroup methyls (V_{CC3}), the remaining phosphocholine (V_{PCN}), the carbonyl-glycerol (V_{CG}), the chain terminal methyls (V_{CH3}) and the double-bonded methines on the chains (V_{CH1}). It may be noted that, contrary to a supposition in the literature (Wiener and White, 1991), the moiety distribution functions do not have to be Gaussians, although simulations show that Gaussians are fairly accurate for the headgroup moieties. Except for the terminal methyl whose position is constrained to the center of the bilayer, each Gaussian has three parameters for its position, height and width. Then, the distribution function $v_{CH2}(z)$ for the chain methylenes is $V_{HC}(z)$ minus $V_{CH3}(z)$ and $V_{CH1}(z)$. These parameters directly give D_B and then the measured volume V_L determines A_L via Eq. (1). Eq. (3) also provides a constraint.

A fitting routine then finds the values of the parameters P in the model that minimizes, for both x-ray and neutron data, the differences between the model $F_P(q)$ and the data $F_d(q)$ at all values of q_z.

$$\chi^2 = \sum_q \sigma_q^{-2}(|KF_d(q)|^2 - |F_P(q)|^2)^2 + W. \tag{5}$$

Each data point has estimated uncertainties σ_q, and K is a fitting parameter for each data set to take into account unknown scaling factors. The fit can be guided by the final W term, which allows a Bayesian *a priori* target for a selected subset of the P parameters with a penalty W calculated for quadratic differences from their target values. In addition to such soft constraints, a subset of the P parameters can be hard constrained simply by fixing them. The SDP program used for the fluid phase results in Table 1 allows constraining some combinations of parameters, like moiety volumes or the distances between two moieties.

Of course, the goodness of fit depends on the model and the constraints that are applied to the parameters. Too few free parameters do not provide good fits to the form factors, thereby indicating that something important is missing in the model or that too many constraints were applied. However, adding more detail to the model adds more fitting parameters and then the values of the fitted parameters that are important for the moieties can become ill-determined and even meaningless; for example, the methine parameters were ill-determined and were therefore constrained. Such behavior has three causes. One is that the data are not perfect, so the model tries to fit spurious, noisy values. Second, the model is not perfect; there is no reason that the probability distribution functions are Gaussians or any other analytic form. Third, the distribution of the moiety electrons is not likely to be uniform within the moiety volume. These causes make it reasonable to steer the model by using outside information and intuition in a Bayesian way that assigns a plausible target value for some of the parameters with an assignable quadratic penalty term. For example, stereochemical constraints, such as the distance between the hydrocarbon mean boundary D_C and the center of the CG moiety, can be applied. While this raises the vexing issue of how to choose the constraints, it is likely that deviations from true values will be in the same direction for different samples, so structural differences will still be adequately estimated.

Before getting into more details of the fitting in the next subsection, it

is appropriate to emphasize the importance of the neutron data, despite its being limited to a relatively small range in q_z. Fig. 4 shows the best model fit to the neutron data using both neutron and x-ray data. It also shows a fit when area A_L was constrained to be larger than the best value. Clearly, A_L is very sensitive to neutron data. The reason is that the real space neutron contrast in Eq. (3) is closely related to the D_B thickness, and then $A_L = 2\ V_L/D_B$ from Eq. (1). The x-ray contrast is greatest in the headgroup region, so it focuses on D_{HH}. Often there is an unfortunate and not understood conflict in the values of A_L that fit the x-ray data best, that fit the neutron data best, and that best fit the neutron plus the X-ray data, as is illustrated in Fig. 5. Interestingly, such differences also occur in simulations (Braun et al., 2013). For the X&N combined fit and the results in Table 1, the neutron and x-ray were weighted to give them equal importance by adjusting the overall uncertainties such that the individual reduced χ^2_x and χ^2_n were nearly equal.

The SDP parsing has also been applied to X-ray scattering intensities from unoriented MLV samples (Heftberger et al., 2014). Values of the parameters agree well with other SDP determinations. This approach bypasses direct determination of $F_e(q_z)$ and first obtains a modeled electron density profile from which $F_e(q_z)$ is then obtained (Ollila and Pabst, 2016).

3.2. Detailed examples of modelling

This subsection illustrates how the results of the modelling generally described in the previous subsection depend upon different constraints that can be applied. For this section I have used the best available x-ray data of my group. Over the years we have taken many X-ray data sets for DOPC because we used this lipid as our control each time we went to the synchrotron. Ten such data sets are averaged in Fig. 3 and this has allowed a better estimate of experimental uncertainties than is typical for other lipids. A detailed analysis of these data combined with DOPC neutron data (Kucerka et al., 2009) and x-ray data from unilamellar vesicles has only been published as supplementary material in (Braun et al., 2013). Before getting into the details, a salient conclusion is that my current estimate of A_L for DOPC (68.7 ± 0.5 Å^2) is considerably smaller than the even earlier value (72 Å^2) obtained from analysis of X-ray data alone (Kucerka et al., 2005).

Table 3 compares results from updated fits to four different models, abbreviated F1, F2, F3 and F4, to the X-ray and neutron data using the SDP software program with the SDP parsing of the lipid. The F1 fit used a soft constraint, displayed as V_{CG}* in Table 3, on the fraction (0.48) of the headgroup volume V_H taken up by the volume of the carbonyl glycerol moiety that was obtained from a simulation (Kucerka et al., 2008). The fitted value in the V_{CG} entry was obtained by minimizing the sum of the residuals between the fit of the data plus the penalty function W (see Eq. (5)) that allowed a different V_{CG} from the Bayesian target value V_{CG}*. The much smaller ensuing V_{CG} fit the data much better but the penalty function in the row designated "soft %" was a large 26% of the total χ^2. This suggests that a smaller target V_{CG}* should be chosen and this is the primary difference in the F2 fit in Table 3, which has much smaller reduced χ^2. The inset of Fig. 3 shows that the F2 fit is much better for the high q x-ray data. (It may be noted that the DOPC values in Table 1 are from supplementary material that was prepared with Norbert Kucerka; those values are essentially the same as for the F2 model in Table 3.)

Table 3
Values of structural parameters described in the text for fits F1-F4. Units are appropriate powers of Å. Hard-constrained values are indicated by ** and soft constraints by *. The measured V_L= 1303 Å^3 was hard constrained. Temperature was 30 °C.

	F1	F2	F3	F4
χ^2_{red}	2.77	1.84	1.69	1.72
soft %	26	4	5	0
A_L	67.8	68.7	69.8	68.1
D_B	38.5	37.9	37.4	38.3
$2D_C$	28.7	28.3	27.8	28.0
W_C	2.6*	2.5	3.2**	2.4
D_{HH}	35.0	36.0	36.4	36.2
$2Z_{PCN}$	37.0	39.6	39.4	39.0
W_{PCN}	3.1	2.5	1.9	2.2
Z_{CC3}	19.5	20.6	20.0	19.8
W_{CC3}	3.2	2.4	1.5	2.2
Z_{CG}	15.6	15.4	15.2	15.3
W_{CG}	2.8	2.8	2.4	2.5
V_H	331**	331**	331**	350
V_{CG}*	159*	119*	132*	126*
V_{CG}	140	112	114	126
V_{PCN}	88	89	91	94
V_{CH2}	27.3	27.4	27.7	26.9
$r = V_{CH3}/V_{CH2}$	1.98	1.94	1.88	1.93
$Z_{CC3} - Z_{PCN}$	1.0	0.8	0.3	0.3
$D_{HH}/2 - D_C$	3.2	3.9	4.3	4.1
$Z_{PCN} - D_C$	4.2	5.6	5.8	5.5
$Z_{CG} - D_C$	1.3*	1.3*	1.3*	1.3*
N_I	11.6	11.9	12.2	11.0

Fig. 6 shows the electron density profiles for the F2 fit. The positions of the headgroup Gaussians Z_{CG} (carbonyl-glycerol), Z_{PCN} (phosphocholine minus the headgroup methyls) and Z_{CC3} (headgroup methyls) and their widths (W_{CG}, W_{PCN} and W_{CC3}) are reasonable. Especially important is that the water profile conforms to expectations, going to zero along with the CG profile as they approach the hydrocarbon region. The difference $Z_{CC3} - Z_{PCN}$ is small for all four fits, which is consistent with NMR (Seelig and Seelig, 1980) and neutron diffraction

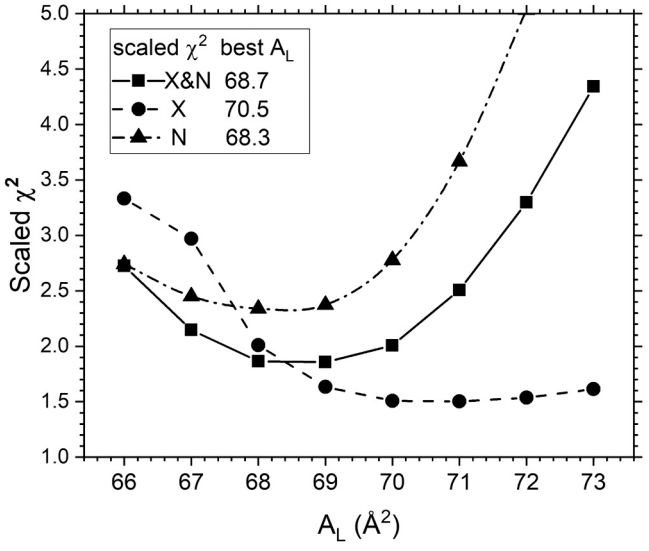

Fig. 5. Comparing DOPC reduced χ^2 for X-ray (X), neutron (N) and both (X&N) data with fixed values of A_L. χ^2_X and χ^2_N have been scaled for better viewing.

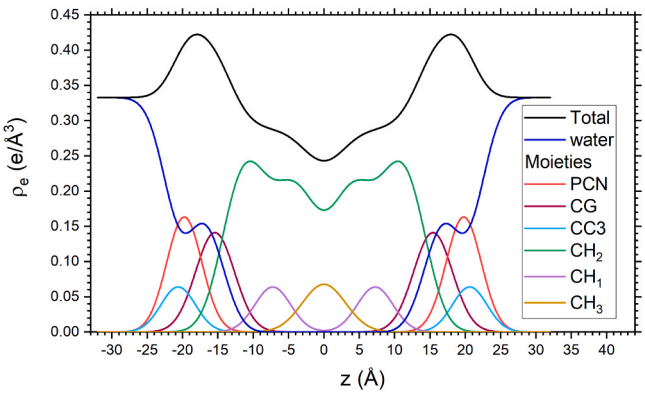

Fig. 6. Electron density profile of DOPC and its moieties from F2 fit in Table 3.

(Buldt et al., 1979) results that the PC dipole is nearly perpendicular, rather than parallel, to the bilayer normal. The distance $Z_{CG} - D_C$ was softly constrained, but freeing that constraint, while only moving it to 0.88 and reducing χ^2 to 1.81, gave an unrealistically small W_{CC3}. Note that the double bond width and position were constrained as shown in Fig. 6 because they become unreasonable and erratic when allowed to be free.

The F3 fit in Table 3 explores increasing the width W_C of the hydrocarbon interface. Although the reduced χ^2 decreases compared to F2, the width W_{CC3} of the headgroup methyls is too narrow, and the water extends rather further into the hydrocarbon region than the CG group. This unrealistic trend continues with even wider and unconstrained W_C, so F3 is as far as I would contemplate going in this direction. Notably, A_L increases by about 1 $Å^2$ compared to F2, which had also increased by about 1 $Å^2$ from F1.

Although the volumetric analysis (Nagle et al., 2019b) finds that the PC headgroup volume is no larger than 331 $Å^3$, a considerably larger value has recently been reported from analysis of x-ray scattering from monolayers (Harvey et al., 2023). Those data were interpreted by an analysis quite similar to this LAXS analysis. The possibility of a larger V_H for the bilayer data here is explored in the F4 fit that minimized χ^2 with the same constraints used in F2. Like F3, the χ^2 is smaller than F2, but unlike F3, the volume probability widths look reasonable. This recent development suggests that there is a conflict between the volumetric analysis and this LAXS analysis that has not been resolved.

Comparing the four fits in Table 3, D_B decreases with increasing A_L as required by Eq. (1). and the highly precise experimental V_L. The hydrocarbon thickness $2D_C$ also decreases with increasing A_L for the first three fits, but it also decreases for F4 because the hydrocarbon $V_C = V_L - V_H$ is smaller due to the larger V_H. Also expected is that D_{HH} should be smaller than $2Z_{PCN}$ because the former comes from the sum of the PCN and CG Gaussians. It is expected that D_{HH} and $2Z_{PCN}$ are generally independent of A_L.

An especially important result is for $D_{H1} = (D_{HH}/2 - D_C)$, which has been fixed to gel phase results in pre-2008 analysis. Its value for the F2-F4 fittings at about 4 Å is significantly smaller than its value of 5.4 Å for the DPPC gel phase in Table 5, and constraining to that latter value accounts for the previously larger value of $A_L = 72$ $Å^2$ for DOPC. If one supposes that the electron-dense phosphate exclusively determines D_{HH}, then these differences would imply different headgroup structures in the gel and fluid phases. However, as noted above, Z_{PCN} is larger than D_{HH}, so perhaps it is $Z_{PCN}/2 - D_C$ that should be compared to the gel phase. Assuming that Z_{PCN} is the same as half the distance between phosphates on opposite monolayers $D_{PP}/2$, the value of D_{H1} for the F2-F4 fits averages to 5.6 Å, which is the same value one obtains for the gel phase (*vide infra*). This agreement is consistent with the same structure of the headgroup in the gel and fluid phases. This sheds new light on the earlier disagreement for A_L of DOPC.

This case study using the best available scattering data shows that fitting models is complicated, but that uncertainties can be estimated by scrutinizing and varying the constraints that are necessary for fitting realistic models. However, it is important to recognize that the uncertainties are likely to be correlated, so using the same constraints on two different bilayers will move the structural parameters in the same direction compared to using a different set of constraints. Thus, the differences between results for the fluid phases of different lipids in Table 1 are likely to be more accurate than if one were to assign reasonable uncertainties to each lipid and then assign the sum of those uncertainties to the differences. This supports the discussion of those differences that are given in Section 2.

3.3. Selective deuteration

Important early work used neutron diffraction on DPPC that was deuterated on specific moieties (Buldt et al., 1979; Zaccai et al., 1979). A concern is that the D spacing of the most fully hydrated sample was only 54.1 Å compared to fully hydrated D spacings in the range 63–67 Å. The sample had 25% water, which would only be 13.6 waters per lipid compared to the fully hydrated $N_w = 30$ (Nagle and Tristram-Nagle, 2000), but it was a powder sample, so some of the water resided in pools between the MLVs rather than all between the bilayers. The value $A_L = 57$ $Å^2$ was reported for the F phase at T = 50 °C, although our reanalysis indicated $A_L = 63$ $Å^2$ (Nagle et al., 1996), in good agreement with the subsequently obtained values shown in Table 1. The results for the specifically deuterated C_α, C_β and C_γ carbons showed that the PC headgroup is oriented essentially parallel to the surface of the bilayer. The reported position 12.2 Å of the C-4 chain carbon is most closely relatable to $D_C = 14.5$ Å in Table 1, where the difference is due to the C-3 and C-2 methylenes. It would be wonderful if specifically deuterated lipids could be used for more modern neutron experiments on fully hydrated samples, but it is expensive to synthesize the lipids and more scarce neutron beam time would be required to obtain the intensity data for many analogues of the same lipid bilayer, so this method has not been used for many other lipids.

3.4. Simulations

Simulations are capable of providing well-equilibrated, fully hydrated fluid-phase structures in greater detail than any of the modeling in the previous subsections. Of course, the force fields driving the simulations have to be validated by comparing the results to experiment. If such validation can be obtained, then simulations would provide an attractive model-free alternative (Klauda et al., 2006) to the modelling approach in Section 3.1. There are many force fields, and development is ongoing. A thorough review of simulations is beyond the scope of this review, so this section will be limited to remarks about how simulations can interface with structural data and how a suite of simulations compare with the preceding F2 model. This leads to my current suggestions for DOPC structural parameter values, but first some methodological details are reviewed.

There is a very important point regarding the best way to compare simulations to experiments. The results of simulations should be put in forms that compare to the actual form factor and order parameter data instead of to quantities that have been derived from these data. To be specific, area per lipid A_L is typically reported in experimental x-ray, neutron and NMR papers. Since A_L is a very important quantity and since it is the most obvious quantity to obtain from simulations, it is tempting to make it an important basis for comparison. However, it has been emphasized in subsection 3.2 that determining A_L from experiment involves assumptions and modelling, and different authors can obtain different values of A_L from the same data. In contrast, obtaining simulated form factors $F_e(q_z)$ and $F_n(q_z)$ is obtained by straightforward Fourier transformations of the simulated distribution functions for the coordinates along the bilayer normal of all the atoms or moieties in an equilibrium ensemble of snapshots. (I recommend the SIMtoEXP software package (Kucerka et al., 2010) for this; it also uses the atomic form factors that make a difference at high q.)) Therefore, as has been appreciated in many simulation papers (Ollila and Pabst, 2016; Lee et al., 2014; Dickson et al., 2022; Ollila et al., 2023; Jambeck and Lyubartsev, 2012; Poger et al., 2016; Tjornhammar and Edholm, 2014; Klauda et al., 2010), the x-ray and neutron form factors and the NMR order parameters are the structural data to which simulations should be compared, not the A_L that experimental papers love to derive.

There are artifacts to avoid when obtaining real-space electron density and neutron scattering length profiles from simulations. Most obviously, the entire bilayer may move in the z-direction during a long simulation. To avoid smearing the profiles, which makes $F(q_z)$ decay too rapidly with increasing q_z, snapshots must be repositioned to a common average zero position. A more subtle smearing of the profiles occurs in simulations consisting of many lipids because then the membrane is laterally large enough that each snapshot has undulations that also smear the average profile, and then the Fourier transform would not

correspond to the experimental $F(q_z)$ which pertain to flat, non-undulating bilayers. On the other hand, simulating with fewer lipids runs the risk that periodic boundary conditions in the in-plane direction create artifacts. Methods to account for the undulation artifact have been devised (Braun et al., 2011), and it was shown in a study of DMPC that 64 lipids appeared to be enough to mostly alleviate the finite size artifact, and 128 lipids appeared to be small enough to alleviate the undulation artifact. Undulations also made the true area per molecule A_L greater than the projected area that is obtained from the average area of the simulation box, although only on the order of 1% when there are 1024 lipids. After artifacts have been controlled, the atomic or moietic distribution functions can be obtained in bins in the z direction, typically 0.02 nm high to obtain smooth real space profiles.

Given that force field fields are generally imperfect, I suggest the following workaround when agreement with the experimental form factor data is poor. Experimental bilayer systems have no deliberate surface tension γ, which implies that the simulations should be performed in the NPT ensemble with $\gamma = 0$. However, while the hydrocarbon region is likely well described by current force fields, the interfacial region is likely less well described due to the omission of the quantum mechanics of hydrogen bonding of water and polarizability (although polarizability is now being accommodated in the Drude approximation (Yu et al., 2023)). This suggests that using either NPAT or NPγT with a non-zero surface tension could be a model-free workaround (Braun et al., 2013; Klauda et al., 2006; Nagle, 2013) to obtain better agreement with experimental data (Braun et al., 2013; Marquardt et al., 2020; Allsopp et al., 2022; Neale et al., 2015; Raghunathan et al., 2012; Kučerka et al., 2008). The ensuing values of A_L and other structural parameters would then be the values obtained from this force field. This work-around has been described as a model-free method (Klauda et al., 2006) in the sense that it is independent of the type of modelling in Sections 3.1 and 3.2; of course, the model in simulations is the force field itself.

Many force field studies in the past have compared to only one or a subset of lipid bilayer experiments. This can be misleading. The parameters in a force field may be tuned to agree well with one experimental property, but those parameters may give results that agree poorly with a different property. A case study of the GROMOS 43A1-S3 force field applied to DOPC illustrated these issues (Braun et al., 2013). The value of A_L that best fit the X-ray form factor was about 2 Å^2 greater than the A_L that best fit the neutron form factor and the NPT simulation gave an A_L that was 0.8 Å^2 smaller than the best neutron A_L, qualitatively similar to what had earlier been reviewed for CHARMM36 simulations (Nagle, 2013). Curiously, this difference in the best values of A_L from x-ray versus neutron form factors is similar to what occurs for modelling in Fig. 5, which might suggest an unknown incompatibility between neutron and x-ray scattering.

After workarounds were made that accommodated differences in water density and lipid volume, it was suggested that the 43A1-S3 force field supported a model-free $A_L = 68.5$ Å^2 for DOPC. Nevertheless, assuming that there is no intrinsic incompatibility of the neutron and x-ray data, the difference in the best values of A_L indicated a force field deficiency. Another indication of a force field deficiency is that even the best fit to the X-ray data had a χ^2_X that was far greater than for the SDP model fit even for the A_L that minimized χ^2_X. In contrast, the neutron χ^2_N was close to 1 for the A_L that minimized it, but that is likely just because the neutron data don't go very far in q_z as shown in Fig. 4. The X-ray data in Fig. 3 go to much larger q_z, so it obtains more fine structure which is a greater challenge for force fields. More positively, this simulation exhibited the same behavior shown in Fig. 2 (as also did a CHARMM36 simulation (Nagle, 2013)), and it had a constant distance between the phosphate and the hydrocarbon interface, consistent with no change in the shape of the headgroup with change in A_L as hypothesized in Fig. 1. To investigate this hypothesis further, it would be interesting to see how the NMR headgroup order parameters behave in simulations in which A_L is varied. Perhaps even more interesting is to determine the A_L that best fits the experimental S_{CD} hydrocarbon chain order parameters.

Turning now to some simulation results, Table 4 compares many structural parameters for DOPC at T = 30 °C from the aforementioned GROMOS 43A1-S3 study and from several newer ones from Venable and Pastor with those from the F2 model fitting in Table 3. As already mentioned, the 43A1-S3 simulation could fit the neutron data very well by tuning the A_L to a smaller value than shown in Table 4 but then χ^2_x is very large, so the A_L in Table 4 was chosen as a compromise. The A_L for the other simulations were obtained using NPT (zero tension) and systems with 72 lipids and no undulation correction. It's clear from comparing the form factors that the best fit to the x-ray data would also be obtained from a considerably larger A_L. Interestingly, it looks like a slightly larger A_L would also decrease χ^2_N, but the best A_L for x-ray data will clearly be larger than the best one for the neutron data as has occurred in the past for CHARMM simulations (Nagle, 2013) as well as for the GROMOS 43A1-S3 study (Braun et al., 2013). It should also be noted that the surface tension workaround mentioned above was used, but only for the GROMOS results, which likely accounts for its smaller reduced χ^2_x compared to the more recemt simulations.

Turning to particulars, the simulations center the double-bonded methines position Z_{CH1} near 7.0 Å, thereby supporting its constrained value in the F2 model. Likewise, the simulations found Z_{CG}-D_C close to the softly constrained 1.3 Å value employed in the F2 model. Agreement for Z_{CG} and D_C individually is also quite good. Agreement in the value of D_B is quite good, consistent with fitting the neutron data reasonably well, except for LJPME which fits the neutron data less well. The Z_{PCN} values are similar in the simulations; the 39.6 Å value obtained by modelling is likely compromised by the spatial overlap of the three headgroup moieties. The more erratic D_{HH} position is related to the widths in the distributions; wider headgroup distributions make D_{HH} smaller because the secondary CG electron density peak pulls the position of the total electron density to lower values than the center of the PCN electron density. In particular, the width of the phosphorus distribution is narrowest for Drude2023 and this accounts for its having the smallest value of Z_{PCN} - $D_{HH}/2$. Together, these help to explain the differences in $D_{HH}/2 - D_C$ and $Z_{PCN} - D_C$; the former is the D_{H1} quantity that was pinned to experimental gel phase values to obtain the values of A_L around 72 Å (Kucerka et al., 2005), which is a procedure that can now be recognized as having been compromised by the effect of the CG distribution on the determination of D_{HH}. The quantity $Z_{PCN} - D_C$ now appears to be the more robust quantity as its value agrees with the gel phase of PC lipids with saturated chains where the distributions are much sharper; indeed $D_{HH}/2$ is only 0.2 Å smaller than the location of the phosphate in the DPPC gel phase (Nagle et al., 2019a).

The simulated total volumes V_L vary somewhat from the highly accurate experimental V_L in the F2 column of Table 4. A method to alleviate this difference, as well as small differences in the density of water was applied to the 43A1-S3 simulations, but that kludge was not employed here. There is general agreement for the ratio r of the terminal methyl to methylene volumes in all the entries in Table 4 and somewhat poorer agreement for the methine to methylene volume; both of these and the variable difference in V_L minus V_H account for the differences in the average methylene volume. The most significant disagreement in volumes is that the F2 model fits the data much better with a smaller V_{CG} than that obtained by the simulations. One possible explanation is simply that the repulsive interactions in the carbonyl/glycerol force fields are too large. Another is that the app in the SIMtoEXP program (Kucerka et al., 2010) that calculates moiety volumes from simulations is flawed because it does not conserve volume at each z level; however, parsing the lipid into separate carbonyl and glycerol moieties conserves volume better, while giving more erratic values for each moiety, but it still gives a similar value for the sum (Nagle et al., 2019b). A third explanation is that the SDP model for the F2 fit is flawed for the reasons discussed in Section 3.2.

Let us come back to the tilt of the PC headgroup that has been mentioned twice before. The out-of-plane angle θ_{PN} of the

Table 4
Comparison of structural parameters of DOPC at 30 C. Units are the appropriate powers of Å and the chi-squares are reduced.

	F2	43A1-S3[a]	C36[b]	LJPME[c]	Drude[d]	Suggested
χ_x^2	1.22	8.3	24.0	12.8	13.6	
χ_n^2	1.16	4.0	4.0	10.7	1.5	
A_L	68.7	68.5	69.2	69.5	69.0	69.0
D_B	37.9	37.8	37.4	36.5	38.0	37.8
$2D_C$	28.3	28.0	28.4	27.8	28.5	28.2
D_{HH}	36.0	36.0	38.0	37.3	37.4	37
$2Z_{PCN}$	39.6	37.8	38.5	38.1	37.6	38.1
$2Z_{CC3}$	41.2	39.6	42.2	41.6	41.8	41.2
$2Z_{CG}$	30.8	30.6	30.4	30.0	30.0	30.4
Z_{CH1}	7.0	7.1	6.9	6.8	6.6	6.9
V_L	1303	1289	1295	1269	1312	1303
V_H	331	334	311	303	331	331
V_{CG}	112	137	146	138	165	132
V_{PCN}	89	89	76	78	87	84
V_{CH2}	27.4	26.7	28.3	28.2	27.3	27.8
$r = V_{CH3}/V_{CH2}$	1.9	2.0	1.9	1.7	2.0	1.9
V_{CH1}/V_{CH2}	0.8	0.9	0.7	0.7	1.0	0.8
$Z_{PCN} - D_{HH}/2$	1.8	0.9	0.3	0.4	0.1	0.5
$D_{HH}/2 - D_C$	3.9	4.0	4.8	4.7	4.4	4.4
$Z_{PCN} - D_C$	5.6	4.9	5.0	5.2	4.6	4.9
$Z_{CG} - D_C$	1.3	1.3	1.3	1.1	1.1	1.2
$Z_{CC3} - Z_{PCN}$	0.8	0.9	1.8	1.8	2.1	1.6
$Z_N - Z_P$		1.0	1.4	1.5	1.8	1.4
θ_{PN}		~13°	20°	20°	23°	18°

[a] = (Braun et al., 2013), [b] = (Nagle et al., 2019b), [c] = (Yu et al., 2021), [d] = (Yu et al., 2023)

phosphocholine headgroup can be defined as $\theta_{PN} = \tan^{-1}((Z_N\text{-}Z_P)/(R_N\text{-}R_P))$, where Z_N and Z_P are the average positions along the bilayer normal of the nitrogen and the phosphorus, respectively, and R_N-R_P is the lateral extent of the P-N vector. Depending on the simulation method, average values of θ_{PN} in the range 15–20° have been reported for the POPC fluid phase (Li et al., 2009; Botan et al., 2015). Although not included in the cited papers, Venable and Pastor have kindly provided for this review full distributions of θ_{PN} values. The fullwidth at half maximum of these distributions is remarkably large, 65° for CHARMM36 and LJPME and 60° for Drude2023; these are consistent with considerable disorder in the headgroup region. The non-zero average values are shown in Table 4 for these three simulations, and a somewhat smaller value is inferred for the GROMOS simulation by comparing its value of $Z_N - Z_P$ to the other simulations. One might try to infer a smaller experimental θ_{PN} by comparing its value of $Z_{CC3} - Z_{PCN}$ to those of the simulations, but it is perhaps more realistic just to emphasize that θ_{PN} is a quantity that is not directly obtainable from scattering data and is best determined by simulations that match the scattering data. In any case, it would seem that non-zero values of θ_{PN} are a refinement compared to the early NMR (Seelig and Seelig, 1980) and neutron diffraction (Buldt et al., 1979) studies that just reported that the PC headgroups are oriented in the plane of the bilayer.

Even though the F2 model gives by far the best fit to the x-ray and neutron data, the values of the structural parameters could be compromised by the collusion of the many parameters in the model that compromises their actual values. I suggest that a sense of the quantitative structure of DOPC can be obtained by examining the similarities with the simulations in Table 4, and a sense of the uncertainties can be obtained by considering the differences. The last column in Table 4 gives my suggested values for the structure of DOPC.

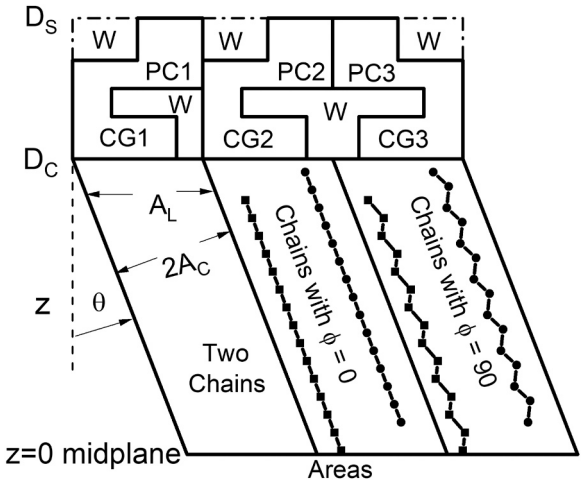

Fig. 7. Cartoon for three molecules in the top monolayer of a gel phase PC lipid bilayer with saturated hydrocarbon chains that are tilted by θ with respect to the bilayer normal. The chain region of the middle molecule #2 shows all-trans hydrocarbon chains with the C-C-C zigzag plane perpendicular to the plane of the paper and molecule #3 shows chains with that plane in the plane of the paper. The methylenes on the *sn*-1 chains have square symbols and circles show the *sn*-2 methylenes. The interfacial region includes water regions labelled W and headgroups with pieces labelled CGn for the carbonyl-glycerol moiety and PCn for the phosphocholine moieties of the n = 1–3 lipids. Chains in the lower monolayer (not shown) would be drawn to be parallel to those in the upper monolayer.

4. Gel phase structure

Results will be described using the cartoon in Fig. 7, which is most pertinent to the gel phase of saturated PC lipids. The first most important difference compared to the fluid phase (and to the cartoon in Fig. 1) is that the hydrocarbon chains are uniformly tilted by θ away from the bilayer normal. The leftmost lipid shows the area per lipid A_L and an important additional area $2A_C = A_L\cos\theta$, which identifies the cross-sectional area A_C per chain *perpendicular* to the chains rather than along the plane of the headgroups. The second and third lipids in the cartoon show hydrocarbon chains with specific azimuthal angles ϕ. Although gel phase chains are usually modelled as cylinders, that supposes complete disorder in ϕ. Supposing that there is an azimuthal order parameter $g = <2\cos^2\phi - 1>$, combining IR results with x-ray results determined g = - 0.3 (Nagle, 1993), which is consistent with a continuous distribution P(ϕ) proportional to $1 + 3\sin^2\phi$. The *sn*-1 chain extends further into the bilayer center than the *sn*-2 chain because the glycerol moiety is perpendicular to the plane of the bilayer (Seelig and

Seelig, 1980), leading to mini-interdigitation of the terminal ends of the chains on the opposing monolayers at the bilayer midplane (Nagle et al., 2019a).

Compared to Fig. 1, the headgroups in Fig. 7 are embellished in a way that has not been previously presented. The locations of the CG and PC moieties are roughly indicated in cartoon fashion, and the interfacial water is non-uniformly distributed in more than one compartment. Although each of the headgroups has an orientation, the orientation of the third lipid is drawn opposite to that of the other two lipids to indicate randomness in the headgroup in-plane orientation (Sun et al., 1994).

Table 5 assembles some pertinent results for understanding the structure of the gel phase. The first important result is that DPPC and DMPC chains tilt, and DLPE chains do not. The second is that A_C is nearly the same for DPPC, DMPC and DLPE. The third important result is that A_L is nearly the same for PC lipids and considerably smaller for DLPE. The data for the three lipids with saturated chains indicate that the hydrocarbon chains are in their straight *all-trans* conformation, so D_C is the *all-trans* chain length of 1.27 Å per methylene times cos θ plus an additional steric length for the terminal methyl.

These results are understandable in light of the competition between heads and chains. Most simply stated, gel phase chains minimize their free energy by packing with cross-sectional area A_C, whereas the heads have a hard-core packing area A_H, below which they strongly resist lateral compression. When A_H is larger than $2A_C$, then the chains tilt to keep their free energy low by reducing the distance between them, while the heads determine the area/lipid A_L to be A_H. Although one could imagine an A_L even larger than A_H with even more chain tilt, tilting incurs a free energy penalty because the ends of the chains have fewer nearest neighbors, so the chains would exert a force to reduce A_L to A_H. Also, the hydrophobic interaction of water with hydrocarbon exerts a strong lateral pressure to minimize A_L. (This hydrophobic lateral pressure is overcome in the fluid phase by the disordering of the chains, which then forces a larger area than A_H.) The cartoon of the headgroup in Fig. 7 was drawn so that it is the PC moiety that has the largest lateral cross-sectional area, making it responsible for chain tilting in PC lipids. This is consistent with the much smaller A_L of DLPE. Both DLPE and the saturated PC lipids have the same CG moieties, whereas the PE moiety of the DLPE headgroup is smaller than for PC due to its having only three hydrogens instead of three methyls, so its hard-core packing area A_H would be smaller, allowing for smaller A_L and negligible chain tilt.

Importantly, the hard core steric areas for the lipids shown in the A_L column in Table 5 are much smaller than the areas of their fluid phases in Table 1. Notably, that means that the smaller A_L of PE lipids in the fluid phase compared to PC lipids in Table 1 is not caused by its smaller steric headgroup. More likely causes that reduce the area of PE lipids in the fluid phase are (i) weak and transient hydrogen bonding of the amino group to an oxygen on a neighboring phosphate group (Nagle, 1980) and (ii) shielding contact of water to the hydrocarbon region by the PC methyls. These would also be reasons that PE lipids have large negative spontaneous curvature (Rand et al., 1990) rather than the smaller steric size of the PE headgroup.

In passing, it may also be noted that the values of A_C in Table 5, excepting DEPC (diC22:1cisPC), are about 20 $Å^2$, significantly larger than the average 18.5 $Å^2$ for crystalline alkanes (Small, 1986). However, crystalline alkanes have fixed azimuthal angle ϕ, whereas gel phase chains have considerable azimuthal disorder which is expected to increase A_C just as in the alkane rotator phase which occurs in a narrow temperature range below the main fluidizing alkane transition (Small, 1986). It is the alkane rotator phase that is most analogous to the lipid gel phase. While both lipids and alkanes have a pretransition and a main transition, the sequence of alkane phases is crystal/rotator/fluid rather than gel/ripple/fluid.

Additional evidence supporting this tilting scenario is that, with increasing temperature, A_C increases, θ decreases and A_L remains nearly the same (Sun et al., 1996a). This is readily explained by thermal expansion of A_C against a soft van der Waals cohesive energy between chains, allowing θ to decrease while various lateral pressures keep A_L close to its hard-core minimum. Furthermore, at the same temperature, as the saturated chain length decreases, A_C increases, θ decreases and A_L remains nearly the same. This is explained by the energy penalty of tilting chains which tries to reduce θ and thereby competes against the cohesive energy. The former is the same for all chain lengths while the latter is proportional to the chain length, so the total free energy minimum moves to smaller θ as chain length decreases (Tristram-Nagle et al., 1993).

Coming back to the DEPC entry in Table 5, its A_L value is nearly the same as for DMPC and DPPC, which is consistent with this discussion. However, there is even closer packing of chains as indicated by the smaller A_c and the tilt angle is consequently larger. This can be understood because packing the conformational ground state structure of *cis* unsaturated chains has kinks that do not permit azimuthal disorder, so the chain packing would be more crystalline with smaller A_C. It may even be better not to call this a gel phase. It is also noteworthy that DEPC has no ripple phase (Nagle et al., 2019a).

Table 5 also shows the head-head spacing D_{HH} and the hydrocarbon thickness $2D_C$. The latter is twice the effective *all-trans* chain length times cos θ. Half the difference between D_{HH} and $2D_C$ is the measure named D_{H1} that estimates how far the phosphate resides from the Gibbs dividing surface between the hydrocarbon and the interfacial regions; D_{H1} was discussed for the fluid phase in Section 3.2.

An important additional result for DPPC and DMPC is that the chains in the lower monolayer (not shown in Fig. 7) are parallel to the chains in the upper monolayer (Sun et al., 1994). It remains somewhat mysterious why this coupling between the monolayers occurs. Perhaps it is due to the mini-interdigitation, (Nagle et al., 2019a) i.e., overlap of the ends of the *sn*-1 chains as illustrated in Fig. 8, that induces parallel packing of the chains. This issue has been addressed by studying MPPC because the shorter 14 carbon myristoyl M chain in the sn-1 position would presumably extend about the same distance to the bilayer center as the longer 16 carbon palmitoyl sn-2 chain and would therefore not have mini-interdigitation. Remarkably, MPPC doesn't even have a gel phase (Tristram-Nagle et al., 1999). Nor does PMPC (Serrallach et al., 1984), which would be even more expected to have a gel phase with coupled monolayers due to more mini-interdigitation than DPPC. The sequence of MPPC and PMPC phases upon raising the temperature is subgel to ripple to fluid. It was suggested that these lipids have more stable subgel phases due to different conformations of the headgroups, but there has been no experimental follow-up and this is an interesting open question in my opinion.

Another interesting lipid for this consideration is a version of DPPC in which the hydrocarbon chains are in the sn-1 and sn-3 positions, thereby symmetrizing the normal DPPC molecule with respect to the glycerol backbone. Accordingly, neutron diffraction has shown that the chains are equivalent in the bilayer, and this led to the conclusion that the glycerol backbone is parallel rather than perpendicular to the bilayer (Buldt and Dehaas, 1982). The WAXS data indicated chain tilt, but the sample was quite dry, and it looks like it might have been $L_{\beta F}$ gel phase with chains tilted toward next nearest neighbors (Smith et al., 1987).

Table 5
Comparison of some gel phase results.

	T	θ	$2A_C$	A_L	$2D_C$	D_{HH}	D_{H1}	n_I
lipid	°C	°	$Å^2$	$Å^2$	Å	Å	Å	
DPPC (Nagle et al., 2019a)	20	32.0	40.1	47.3	34.4	45.2	5.4	4.7
DMPC (Tristram-Nagle et al., 2002)	10	32.3	39.7	47.0	30.2	40.1	5.0	4.6
DLPE (McIntosh et al., 1986)	20	0	41	41	27	37	5	3.9
DEPC (Nagle et al., 2023)	10	42.5	35.1	47.6	42.2	53.8	5.8	4.8

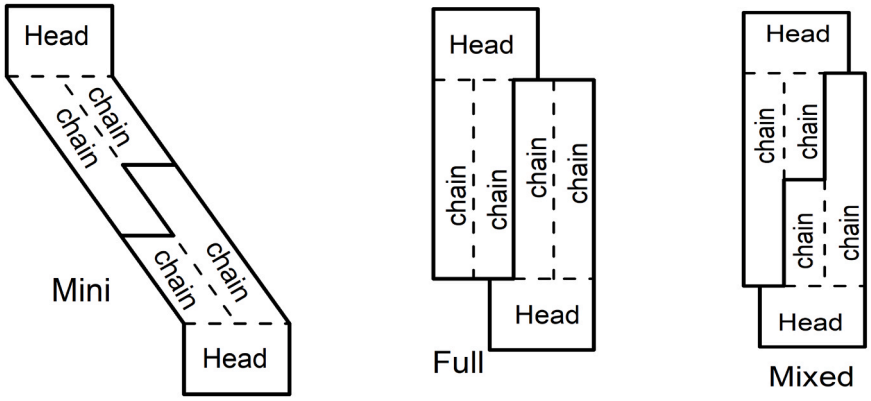

Fig. 8. Types of interdigitation; Mini, Full and Mixed.

Again, this would be an interesting lipid bilayer to study further.

There are other significant gel phase structures that involve different ways that the hydrocarbon chains in the two monolayers interdigitate. The leftmost panel in Fig. 8 illustrates mini-interdigitation that occurs when one chain is effectively longer than the other. As emphasized earlier, the competition between the attractive interaction between chains and the hard core repulsion of the headgroups accounts for tilted parallel chains and maximal headgroup packing. However, the cohesive energy of an array of tilted parallel chains is smaller than if the chains were not tilted.

Fully interdigitated gel phases are cartooned in the middle panel of Fig. 8. This gains back all of the cohesive energy by not tilting the chains and it avoids the hard core headgroup repulsion by fully interdigitating the chains, so $A_L = 4A_C$. But then the headgroup area A_H is generally not large enough to cover all of the terminal methyl ends of the chains ($A_H < 4A_C$), so interdigitation incurs a hydrophobic energy penalty which is evidently large enough to overcome the tilting penalty in DPPC. However, changing the ester linked DPPC to the ether linked DHPC suffices to bring about fully interdigitated gel phases (Matsuki et al., 2007). Furthermore, it has been documented that many small amphipathic molecules, like ethanol, induce a fully interdigitated gel phase when added to DPPC, consistent with the expectation that they would reduce the hydrophobic energy by residing between the headgroups (Kinoshita and Yamazaki, 1996; Huang and McIntosh, 1997). Interestingly, the application of 100 MPa hydrostatic pressure also takes the usual DPPC gel phase into an interdigitated phase (Matsuki et al., 2007). This can be understood qualitatively because pressure would decrease A_C, thereby disfavoring the tilted gel phase by increasing the tilt energy and by favoring interdigitation by decreasing the area exposed to water. A small decrease in the oil/water surface tension under pressure (Hassan et al., 1953) also favors the interdigitated phase.

For mixed chain lipids with more carbons in the sn-1 chain and fewer in the sn-2 chains, increased mini-interdigitation would be expected. However, when the shorter chain is about half the length of the longer chain, a different type of interdigitation occurs (Mcintosh et al., 1984) that is shown in the right panel of Fig. 8. Whereas the fully interdigitated gel phase has four chains per headgroup at each surface, this mixed interdigitation type has only three chains per headgroup. This also maximizes the cohesive chain energy without packing the headgroups too closely together, but by packing them more closely than in the fully interdigitated phase, mixed interdigitation incurs less hydrophobic energy penalty.

These alternatives to the DPPC gel phase structure indicate a subtle interplay between the interactions involved in forming chain-ordered gel phases. However, by far the most research at high resolution has been done on the tilted gel phases of DPPC and DMPC, so the following subsections review some details of how that type of structure was obtained.

4.1. Overview of the basic experimental gel phase structural data

The main systems for gel phase studies are multilamellar arrays and, of these, oriented stacks are advantageous because the data are two dimensional in the scattering vector $\mathbf{q} = (q_z, q_r)$ where q_z is perpendicular to the plane of the bilayers. (Of course, orientation of bilayer stacks is never perfect. Although measurement of mosaic spread is non-trivial (Nagle et al., 2016), it is typically small, less than one degree, and is easily taken into account for the gel phase.) Even though gel phase bilayers have domains with chains all tilted in the same direction, there are so many such domains in the beam that only a radial in-plane q_r is relevant. For DPPC and DMPC gel phase bilayers, the scattering pattern is as shown in Fig. 9. It is also valuable to study MLV samples which are necessarily isotropic. Then, the MLV data consist of uniform rings which are described by only a single q variable; the scattering pattern is obtained by averaging the one in Fig. 9 over rotation of the plane of the paper about the origin.

The right-hand side of Fig. 9 locates the wide-angle scattering (WAXS) that occurs along two Bragg rods. The analysis of these WAXS data gives the values of θ, $2A_C$ and A_L in Table 5 as will be described in the next subsection. It is the precision and analyzability of WAXS scattering that makes it valuable for gel phase structure. The left-hand side of Fig. 9 shows the locations of a regular sequence of Bragg peaks that occur along the locus $q_r = 0$, called the meridian. The q_z values of the peaks index as $q_h = 2\pi h/D$ where D is the lamellar repeat spacing of the

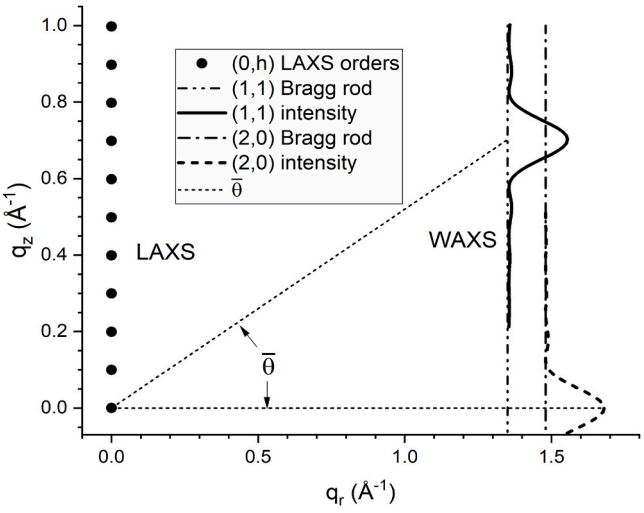

Fig. 9. The general pattern for x-ray scattering from an oriented stack of gel phase DPPC bilayers. LAXS peaks occur at $q_r = 0$. The WAXS intensity is proportional to the horizontal difference between the curved lines and the loci of the vertical Bragg rods.

bilayers in the stack. This scattering is often called SAXS for small angle x-ray scattering, but the angles are not all that small, especially for the recently observed higher h orders (Nagle et al., 2019a), so I prefer the acronym LAXS where the L could stand for Low or, better, the LA could stand for Lamellar. It is the analysis of the intensities in these peaks that gives D_{HH} in Table 5 as well as other aspects of the structure. This analysis is discussed in subsection 4.3.

4.2. Analysis of WAXS data

The first important part of the WAXS analysis is what it excludes. There is no apparent coherent scattering in the WAXS region that would arise from three dimensional in-plane correlations of molecules from different bilayers in multilamellar systems, so the analysis focuses only on a single bilayer. Then, the unit cell is only two-dimensional, although with form factors that depend upon the z-dependence of the electron density. Furthermore, if there were in-plane correlation of headgroups, there would be scattering at smaller q_r values which is not observed (Sun et al., 1994), so the structural analysis involves only the hydrocarbon chains. Also, the scattering is very sharp in the q_r direction (Sun et al., 1994), indicating that in-plane order persists for over 2900 Å. This suggests that the chains are packed very regularly in a single conformation which is assumed to be *all-trans*.

Fig. 10 shows an in-plane rectangular unit cell for the chains with $A_L = ab/2$. For the data pattern in Fig. 9, each chain is tilted towards a nearest neighbor by an angle θ. The q values of the (2,0) and (1,1) peaks give the dimensions of Bragg planes as $d_{20} = 2\pi/q_{20}$ and $d_{11} = 2\pi/q_{11}$. To relate these to the unit cell, define $\delta = \sqrt{(1 - (d_{11}/2d_{20})^2)}$ and then $b = d_{11}/\delta\cos\theta$. When the chain packing is hexagonal, $d_{11} = d_{20}$ and $\delta = \sqrt{3}/2$. Deviations from this value break hexagonal symmetry. Interestingly, this symmetry breaking decreases with increasing temperature and it approaches the same non-zero value for all chain lengths at the lower transition temperature (Sun et al., 1996a). The tilt angle θ is determined because $\delta \sin\theta = \sin\eta$ where η is shown in Fig. 9. These well-known equations (see, *e.g.* Sun et al., 1994) show how just the locations of the WAXS data in q-space provides θ, $2A_C$, and A_L.

More information comes from the intensity as a function of Δq_z from its maximum along the Bragg rods; this is essentially the square of the single slit $\mathrm{sinc}(\Delta z \Delta q_z)$ function, where Δz is the length of the unit that scatters coherently. The result that Δz is twice the length $L\cos\theta$ of *all-trans* chains along the bilayer normal means that the chains in both monolayers are correlated and colinear. The ratio R of the (2,0) to the (1,1) intensity is important as it is unity when the chains are modelled as cylinders, consistent with complete azimuthal averaging of the ϕ angle in Fig. 7. The experimentally determined range R = 0.8 – 1.0 is consistent with a small azimuthal order parameter (Akabori and Nagle, 2014).

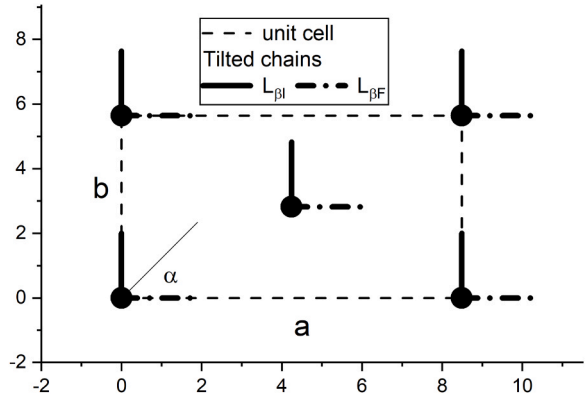

Fig. 10. WAXS unit cell for the $L_{\beta I}$ phase of fully hydrated DMPC with the chains, shown as straight line projections with no azimuthal ϕ dependence, tilted toward nearest neighbors (α=90°) (Tristram-Nagle et al., 2002) and towards next nearest neighbors (α= 0) for the less hydrated $L_{\beta F}$ phase (Smith et al., 1990).

4.3. Analysis of LAXS data – Modelling

The data for structure in the z direction perpendicular to the bilayers are contained in the intensities I_h of the lamellar (q_z=0) peaks, which are conveniently written as

$$I_h = |F_X(q_h)|^2 E(q_h), \quad (6)$$

where $E(q_h)$ is a known factor involving the experimental setup, including the classical Lorentz correction which is roughly 1/q for oriented stacks and $1/q^2$ for unoriented MLVs. In contrast to the fluid phase, the gel phase sample only has form factors $F(q_h)$ at discrete $q_h = 2\pi h/D$ from which one can obtain the real space electron density profile

$$\rho_e(z) = \rho_{eW} + (1/D)\Sigma_h F_X(q_h)\cos(zq_h), \quad (7)$$

where ρ_{eW} is the electron density of the solvent, provided one can determine the signs of $F_X(q_h)$. This is aided by varying the D-spacing which allows sampling the underlying continuous transform as shown in Fig. 11. However, as for the fluid phase, modelling is the best method for obtaining the electron density profile and that automatically provides the signs of the $F_X(q_h)$. The electron densities of the moieties shown in Fig. 7 are shown in Fig. 12 along with the total electron density and its Fourier reconstruction from Eq. (7).

Table 6 shows results for more structural parameters for gel phase DPPC than are given in Table 5. The fitting of the LAXS model additionally gives the volumes of the CG, PC, CH_2 and CH_3 moieties, the latter via the ratio $r = V_{CH3}/V_{CH2}$. The number of water molecules per lipid n_W is the volume $(D - D_B)A_L/2$ for a typical repeat distance D divided by the volume ~30 $Å^3$ of a water molecule. The number of interfacial water molecules n_I is calculated by assuming that the interfacial region is ~10 Å thick. The fitting also obtains D_{HH}, D_B and D_C and it locates the average positions D_{CG} of the CG and $D_{PP}/2$ of the phosphate P moieties. Note that there is a small difference between $D_{PP}/2$ and $D_{HH}/2$ because the latter is essentially the location of the maximum of the sum of two Gaussians. The difference $D_{H1} = D_{HH}/2 - D_C$ has been of interest when discussing the fluid phase. Its value depends upon the conformation of the headgroup. The effective location of the CG group is mostly determined by the carbonyl moieties which are more electron

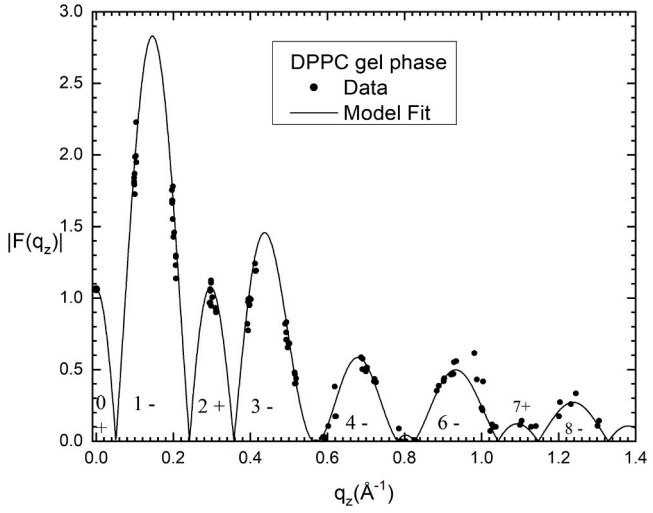

Fig. 11. The discrete $|F(q_z)|$ data and the model continuous $|F(q_z)|$ that bounces off zero as the sign changes between the lobes numbered 1–8 with plus and minus signs indicated for the phase factors. F(0) comes from Eq. (3).

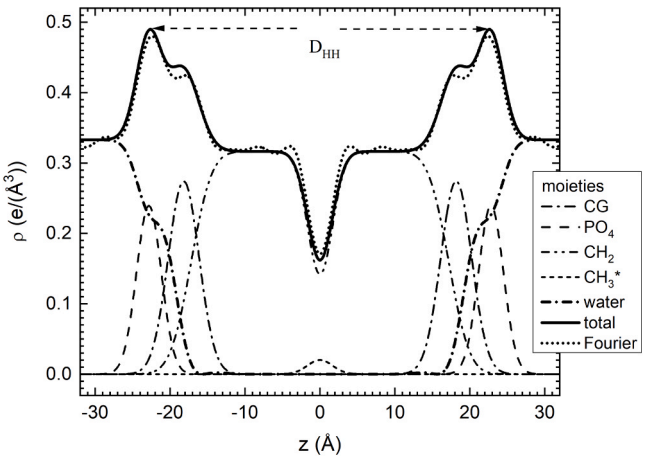

Fig. 12. Electron density profiles of the DPPC gel phase moieties determined from modelling the data in Fig. 7 and its total (solid line) along with the Fourier ρ(z) using Eq. (7). for one value of D.

Table 6
Some more detailed results for DPPC gel phase at 20 °C from (Nagle et al., 2019a). Symbols are defined in the text. Units are the appropriate power of Å.

V_L	1144	V_H	331
V_{CG}	124	V_{PC}	207
V_{CH2}	25.3	r	2.1
A_L	47.3	D	63.3
N_W	11.7	N_I	4.7
$D_B/2$	24.2	$D_{HH}/2$	22.6
D_C	17.2	D_{H1}	5.4
$D_{PP}/2$	22.8	D_{CG}	18.2
$D_{CG} - D_C$	1.0	θ	32.0

dense than the glycerol backbone. Stereochemical models suggest that they are on average located 1.3 Å from their attached methylene groups, so $D_{CG} - D_C$ is an appropriately soft constrained quantity.

4.4. Neutron diffraction results

Neutron diffraction applied to specifically deuterated methylenes on the hydrocarbon chains in the gel phase found that the chains were *all trans* and the *sn*-1 chain went deeper into the bilayer than the *sn*-2 chain (Zaccai et al., 1979), as portrayed in Fig. 7. The positions of the C_α, C_β and C_γ carbons in the choline moiety required that the PC dipole lies more parallel than perpendicular to the plane of the bilayer (Buldt et al., 1979), as is assumed in Fig. 7. Detailed comparison to the results in Table 6 are best done for the 25% water results because the bilayer becomes thicker under the osmotic pressure (Rand and Parsegian, 1989) that occurred in their 6% water results. The location of the C-15 carbon gives a ratio r = 1.8 using $z_{C15} = (r + 0.5)1.27Å\cos\theta$ where the r factor gives the travel of the terminal methyl along the tilted chain and the 0.5 takes one to the center of the C-15 methylene. The location of the C-4 carbon suggests $D_C = z_{C4} + (2 + 0.5)*1.27Å\cos\theta = 18.1$ Å, where the factor of 2 accounts for the C-2 and and C-3 methylenes and the 0.5 factor takes one to the center of the C-4 methylene; this is somewhat larger than in Table 6. If one supposes that the phosphate is located between the GC-3 and C_α carbons to which it is bonded, then one could have $D_{PP}/2 = 22.8$ Å as in Table 6. Finally, it was later emphasized that the glycerol backbone had to be oriented perpendicular to the plane of the bilayer (Buldt and Wohlgemuth, 1981).

Even more complete gel phase structures could be obtained by selectively deuterating other moieties and combining the results with those from x-ray scattering and from neutron scattering from samples with no lipid deuteration, only water deuteration, provided that the same relative humidity is ensured. Extruded unilamellar samples that have been employed for fluid phase bilayers would ensure that, but there would then be a concern for gel phase studies that the long range in-plane lipid chain packing order could be disrupted by incommensurately forcing it into highly curved vesicles.

4.5. Gel phase simulations

The gel phase is especially challenging for simulations because it takes more time to equilibrate than in the fluid phase. As nicely shown recently, cooling from well equilibrated F phases can lead to a variety of gel-like structures with rather larger $A_L \approx 50$ Å^2 and $\theta \approx 36°$ than DPPC experiment (Khakbaz and Klauda, 2018). Earlier simulations started from the crystal structure (Tu et al., 1995; Venable et al., 2000) and respectively obtained somewhat smaller $A_L = 45.8$ and 45.4 Å^2 and $\theta = 33.6°$ and 31.9°. All simulations obtained predominantly all-trans chains but the chains in one monolayer were frequently not parallel to chains in the other monolayer – this is described as pleated - except for (Venable et al., 2000) when the initial configuration had parallel chains which then did not become pleated when run in the constant pressure ensemble but did become pleated in the fixed area ensemble. It remains mysterious what are the interactions that require the direction of tilt of the chains in the two monolayers to be so firmly coupled in experiment in contrast to the simulations.

Besides DPPC Khakbaz and Klauda (Khakbaz and Klauda, 2018) focused more on DMPC for which they reported $A_L = 52$ Å^2 and $\theta = 32.2°$. They also reported $|S_{CD}| = 0.254$. This can be related to the average azimuthal chain angle ϕ. For chain tilt angle θ and a single angle ϕ,

$$S_{CD} = ½(\sin^2\theta(1 + \cos^2\phi) - 1). \quad (8)$$

For $\theta = 32°$, S_{CD} varies from - 0.22 for $\phi = 0$ to - 0.36 for $\phi = 90$, so the ϕ distribution in the simulation leans towards that shown in the middle lipid in Fig. 7. In contrast, the experimental P(ϕ) distribution at the beginning of Section 4 leans towards the third lipid in Fig. 7. Unfortunately, it appears that direct NMR measurement of quantitative values of S_{CD} is not feasible in the gel phase (Barry et al., 1991). In passing, Eq. (8) applies locally to any CD_2 group, even in the fluid phase, but then it is assumed that the azimuthal angle is random so $\langle\cos^2\phi\rangle = ½$ and the molecular order parameter S_{mol}, defined as - $2S_{CD}$, become the usual ½ $(3\cos^2\theta - 1)$ where the travel of the hydrocarbon chain along the normal to the bilayer is cosθ times 1.27 Å. At my request, Venable and Pastor have tested this assumption using CHARMM simulations where it was found to hold very well.

5. Other bilayer phases

The structures of the well hydrated ripple and subgel phases that occur in DPPC and DMPC have been objects of chemical physics research, even though they have limited biological relevance. While one should not be surprised that an even more ordered subgel structure might occur at low temperatures because the headgroups in the gel phase are still disordered, why there is a ripple phase at temperatures between those of the gel phase and the fluid phase remains an intriguing mystery (Nagle, 2023).

5.1. Ripple phase structure

Fig. 13 shows the most highly resolved structure of any ripple phase (Akabori and Nagle, 2015). The bright bands have higher electron density due to the phosphate head groups and the central dark band locates the electron sparse terminal methyl trough. Beginning with the first structural paper (Tardieu et al., 1973) many studies agree that the ripple, surprisingly, has an asymmetrical sawtooth shape, so the repeat pattern has a major, longer side and a shorter minor side. (DPPC also has

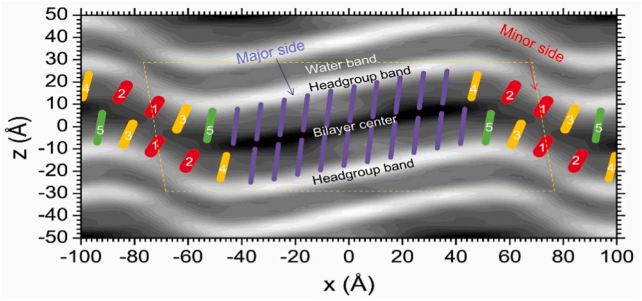

Fig. 13. Structure of the DMPC ripple phase at 18ºC (Akabori and Nagle, 2015) showing one complete bilayer with superimposed colored chains sandwiched between monolayers of two adjacent bilayers in a stack.

a symmetric ripple phase that is metastable with respect to the asymmetric ripple and can complicate data collection (Katsaras et al., 2000), so it has been more convenient to focus on DMPC). The electron density is smaller in the minor side, indicating a larger area per lipid. The sample was an oriented stack, so there is also a lamellar repeat D spacing. Together with the horizontal wavelength λ_r there is a two-dimensional unit cell shown by the faint yellow dashed lines. The unit cell has a monoclinic angle γ that decreases from 98º in Fig. 13 towards 90º as full hydration is approached (Wack and Webb, 1989).

Overlaid in color on this figure are determinations of the orientations and conformations of the hydrocarbon chains. The major side has essentially all-trans chains, colored purple, that are tilted from the normal of the major side by 18º, somewhat less than in the gel phase, and the in-plane unit cell is $L_{\beta F}$ with chains tilted toward next nearest neighbors instead of $L_{\beta I}$ with chains tilted toward nearest neighbors. An analysis of medium resolution data (Wack and Webb, 1989) only found that the major side was gel like (Sun et al., 1996b). A subsequent study (Sengupta et al., 2003) proposed that these chains were oriented along the bilayer normal, unlike Fig. 13, but then a later theoretical paper (Kamal et al., 2011) based on essentially the same data showed the major side chains oriented more like in Fig. 13. The chains in the minor side, colored red, orange and green, are drawn shorter and fatter to indicate that they are conformationally disordered, more like the fluid phase, consistent with the larger headgroup area and the smaller thickness of the minor side compared to the major side.

Obtaining the structure in Fig. 13 involved modelling both the LAXS and WAXS data with similarities to the analysis of the gel phase data. It should be noted that the bilayers in Fig. 13 are quite close to one another because the D spacing was only 58 Å compared to the fully hydrated 67 Å; these were also the conditions of medium resolution data (Wack and Webb, 1989). Structures have not generally been obtained for other hydration levels because the unit cell in Fig. 13 becomes more like a rectangle (there can still be a sawtooth ripple) and then reflections that determine the asymmetric ripple cannot be separated. Also, structures have not been obtained as a function of temperature. It would be interesting to see how the balance between the major and minor sides changes while in the ripple phase as both temperature and humidity are varied.

Periodic boundary conditions pose a difficulty for performing simulations of the ripple phase because of having to choose the number of lipids in the simulation. Having too few lipids prevents the development of a full ripple. Although one could choose that number to conform to experiment, that might not conform to the ripple wavelength that would minimize the free energy using an imperfect force field. Two prominent simulation studies (Khakbaz and Klauda, 2018; de Vries et al., 2005) have reported interdigitation in the minor side which is ruled out in Fig. 13 because the regions of small headgroup electron density (the red lipids) are not spatially opposite in the bilayer. It may be noted that this feature was not built into the modelling but just the opposite. The best fit of the model to the intensities only provided the phase factors which were then combined with the measured intensities to obtain the electron density profile in Fig. 13. It may also be noted that Fig. S14 in (Akabori and Nagle, 2015) suggests a way that elongation of the minor side could introduce interdigitation, and that might come about either from an inaccurate force field or because the Fig. 13 structure was not as fully hydrated as the simulations.

5.2. *Subgel structure*

The conspicuous x-ray feature that identifies the subgel phase is additional reflections for q values between the LAXS and WAXS regions. While that seemed consistent with a packing of four azimuthally oriented DPPC chains into a unit cell compared to two azimuthally averaged chains per unit cell in the gel phase (Ruocco and Shipley, 1982), a study of oriented samples found that the chain packing was essentially unaltered from the gel phase, with the chains tilting only about 2º more relative to the bilayer normal and only about 5º degrees away from nearest neighbors (Katsaras et al., 1995). Instead, the additional peaks were attributed to head group ordering, which had remained disordered in the gel phase, and the in-plane unit cell contains two headgroups that were correlated across the bilayer. Interestingly, that still allowed for six different orientations of the lipid molecules within the in-plane unit cell. It might be noted that, like the ripple phase structure above, the samples were at reduced humidity, so the D spacing was about 5 Å below that at full hydration. However, the q values of the additional reflections were similar to those from fully hydrated MLVs.

Simulations of the subgel phase would likely require crossing large free energy barriers unless the initial state was chosen to be close to the equilibrated one. Also, small discrepancies in the force fields, which would not much affect the fluid phase structure, might give quite different structures than observed.

6. Discussion and conclusions

This review has been confined to single component bilayers as these are the best studied and the most amenable to in-depth analysis and precise results. The fluid and gel phases are the best studied and this is a review of those that were fully hydrated. A major motivation is to test simulations, but this review has emphasized the uncertainties in modeling experimental scattering form factors in inverse Fourier space to provide real space structure. Nevertheless, modeling most likely determines differences in the bilayer structure of different lipids reliably. However, the most precise real space structures for fluid phase lipid bilayers may come from simulations, provided they pass the test of agreeing with the scattering form factors as well as with volumes and NMR order parameters. Force fields that pass these tests would then be likely to provide more reliable and complete model-free structures for lipid mixtures and asymmetric bilayers than can be obtained experimentally. In this review, both modeling and simulations were used to propose detailed structural parameters for DOPC in Table 4.

For the gel phase, in contrast, there are more and better experimental data, so modelling is relatively more certain, while the gel phase is more challenging for simulations. However, there are still uncertainties about the structure of the gel phase, and many more uncertainties about the other low temperature phases.

CRediT authorship contribution statement

John F. Nagle: Writing – review & editing, Writing – original draft, Methodology, Formal analysis, Data curation, Conceptualization.

Declaration of Competing Interest

The authors declare that they have no known competing financial interests or personal relationships that could have appeared to influence the work reported in this paper.

Acknowledgements

I am pleased to acknowledge Chen Shen, Frank Heinrich, Norbert Kucerka and Richard Pastor for careful, critical readings and very helpful comments. I thank Richard Venable and Richard Pastor and for providing several pieces of unpublished specific information at my request, and especially for providing recent simulations in the SIMtoEXP format for Section 3.4. This research did not receive any specific grant from funding agencies in the public, commercial, or not-for-profit sectors.

Appendix A. Supporting information

Supplementary data associated with this article can be found in the online version at doi:10.1016/j.chemphyslip.2026.105577.

Data availability

The data in Fig. 3 are available in Supplementary Material.

References

Akabori, K., Nagle, J.F., 2014. Comparing lipid membranes in different environments. ACS Nano 8, 3123–3127.
Akabori, K., Nagle, J.F., 2015. Structure of the DMPC lipid bilayer ripple phase. Soft Matter 11, 918–926.
Allsopp, R., Pavlova, A., Cline, T., Salyapongse, A.M., Gillilan, R.E., Di, Y.P., Deslouches, B., Klauda, J.B., Gumbart, J.C., Tristram-Nagle, S., 2022. Antimicrobial peptide mechanism studied by scattering-guided molecular dynamics simulation. J. Phys. Chem. B 126, 6922–6935.
Barry, J.A., Trouard, T.P., Salmon, A., Brown, M.F., 1991. Low-temperature deuterium NMR spectroscopy of phospholipid bilayers containing docosahexaenoyl (22: 6. omega. 3) chains. Biochem. -Us 30, 8386–8394.
Botan, A., Favela-Rosales, F., Fuchs, P.F., Javanainen, M., Kanduc, M., Kulig, W., Lamberg, A., Loison, C., Lyubartsev, A., Miettinen, M.S., 2015. Toward atomistic resolution structure of phosphatidylcholine headgroup and glycerol backbone at different ambient conditions. J. Phys. Chem. B 119, 15075–15088.
Braun, A.R., Brandt, E.G., Edholm, O., Nagle, J.F., Sachs, J.N., 2011. Determination of electron density profiles and area from simulations of undulating membranes. Biophys. J. 100, 2112–2120.
Braun, A.R., Sachs, J.N., Nagle, J.F., 2013. Comparing simulations of lipid bilayers to scattering data: the GROMOS 43A1-S3 force field. J. Phys. Chem. B 117, 5065–5072.
Buldt, G., Dehaas, G.H., 1982. Conformational differences between Sn-3-phospholipids and Sn-2-phospholipids - a neutron and X-ray-diffraction investigation. J. Mol. Biol. 158, 55–71.
Buldt, G., Gally, H.U., Seelig, J., Zaccai, G., 1979. Neutron-diffraction studies on phosphatidylcholine model membranes.1. head group conformation. J. Mol. Biol. 134, 673–691.
Buldt, G., Wohlgemuth, R., 1981. The headgroup conformation of phospholipids in membranes. J. Membr. Biol. 58, 81–100.
de Vries, A.H., Yefimov, S., Mark, A.E., Marrink, S.J., 2005. Molecular structure of the lecithin ripple phase. P Natl. Acad. Sci. 102, 5392–5396.
Dickson, C.J., Walker, R.C., Gould, I.R., 2022. Lipid21: complex lipid membrane simulations with AMBER. J. Chem. Theory Comput. 18, 1726–1736.
Doktorova, M., Kucerka, N., Kinnun, J.J., Pan, J.J., Marquardt, D., Scott, H.L., Venable, R.M., Pastor, R.W., Wassall, S.R., Katsaras, J., Heberle, F.A., 2020. Molecular structure of sphingomyelin in fluid phase bilayers determined by the joint analysis of small-angle neutron and X-ray scattering data. J. Phys. Chem. B 124, 5186–5200.
Frewein, M., Doktorova, M., Pabst, G., 2021. Structure and interdigitation of chain-asymmetric phosphatidylcholines and milk sphingomyelin in the fluid phase. Symmetry 13, 1441.
Harvey, R.D., Bello, G., Kikhney, A.G., Torres, J., Surya, W., Wölk, C., Shen, C., 2023. Absolute scattering length density profile of liposome bilayers obtained by SAXS combined with GIXOS: a tool to determine model biomembrane structure. J. Appl. Crystallogr 56, 1639–1649.
Hassan, M.E., Nielsen, R.F., Calhoun, J.C., 1953. Effect of pressure and temperature on oil-water interfacial tensions for a series of hydrocarbons. T Am. I Min. Met Eng. 198, 299–306.
Heftberger, P., Kollmitzer, B., Heberle, F.A., Pan, J., Rappolt, M., Amenitsch, H., Kučerka, N., Katsaras, J., Pabst, G., 2014. Global small-angle X-ray scattering data analysis for multilamellar vesicles: the evolution of the scattering density profile model. Appl. Crystallogr. 47, 173–180.
Huang, C., McIntosh, T.J., 1997. Probing the ethanol-induced chain interdigitations in gel-state bilayers of mixed-chain phosphatidylcholines. Biophys. J. 72, 2702–2709.
Jablin, M.S., 2015. Tilt-dependent analysis of diffuse X-ray scattering from oriented stacks of fluid phase lipid bilayers. Diss. Carne Mellon Univ. 257.
Jambeck, J.P.M., Lyubartsev, A.P., 2012. Derivation and systematic validation of a refined all-atom force field for phosphatidylcholine lipids. J. Phys. Chem. B 116, 3164–3179.
Kamal, M.A., Pal, A., Raghunathan, V.A., Rao, M., 2011. Theory of the asymmetric ripple phase in achiral lipid membranes. Epl-Eur. Lett. 95.
Katsaras, J., Raghunathan, V.A., Dufourc, E.J., Dufourcq, J., 1995. Evidence for a 2-dimensional molecular lattice in subgel phase dppc bilayers. Biochemistry 34, 4684–4688.
Katsaras, J., Tristram-Nagle, S., Liu, Y., Headrick, R.L., Fontes, E., Mason, P.C., Nagle, J. F., 2000. Clarification of the ripple phase of lecithin bilayers using fully hydrated, aligned samples. Phys. Rev. E 61, 5668–5677.
Khakbaz, P., Klauda, J.B., 2018. Investigation of phase transitions of saturated phosphocholine lipid bilayers via molecular dynamics simulations. Biochim. Et. Biophys. Acta-Biomembr. 1860, 1489–1501.
Kinoshita, K., Yamazaki, M., 1996. Organic solvents induce interdigitated gel structures in multilamellar vesicles of dipalmitoylphosphatidylcholine. Biochim. Et. Biophys. Acta-Biomembr. 1284, 233–239.
Klauda, J.B., Kucerka, N., Brooks, B.R., Pastor, R.W., Nagle, J.F., 2006. Simulation-based methods for interpreting X-ray data from lipid bilayers. Biophys. J. 90, 2796–2807.
Klauda, J.B., Venable, R.M., Freites, J.A., O'Connor, J.W., Tobias, D.J., Mondragon-Ramirez, C., Vorobyov, I., MacKerell, A.D., Pastor, R.W., 2010. Update of the CHARMM All-atom additive force field for lipids: validation on six lipid types. J. Phys. Chem. B 114, 7830–7843.
Koenig, B.W., Gawrisch, K., 2005. Specific volumes of unsaturated phosphatidylcholines in the liquid crystalline lamellar phase. Biochim. Et. Biophys. Acta-Biomembr. 1715, 65–70.
Kucerka, N., Gallova, J., Uhrikova, D., Balgavy, P., Bulacu, M., Marrink, S.J., Katsaras, J., 2009. Areas of monounsaturated diacylphosphatidylcholines. Biophys. J. 97, 1926–1932.
Kucerka, N., Heberle, F.A., Pan, J.J., Katsaras, J., 2015b. Structural significance of lipid diversity as studied by small angle neutron and X-ray scattering. Membranes 5, 454–472.
Kucerka, N., Katsaras, J., Nagle, J.F., 2010. Comparing membrane simulations to scattering experiments: introducing the SIMtoEXP software. J. Membr. Biol. 235, 43–50.
Kucerka, N., Nagle, J.F., Sachs, J.N., Feller, S.E., Pencer, J., Jackson, A., Katsaras, J., 2008. Lipid bilayer structure determined by the simultaneous analysis of neutron and x-ray scattering data. Biophys. J. 95, 2356–2367.
Kucerka, N., Nieh, M.P., Katsaras, J., 2011. Fluid phase lipid areas and bilayer thicknesses of commonly used phosphatidylcholines as a function of temperature. Biochim. Et. Biophys. Acta-Biomembr. 1808, 2761–2771.
Kucerka, N., Tristram-Nagle, S., Nagle, J.F., 2005. Structure of fully hydrated fluid phase lipid bilayers with monounsaturated chains. J. Membr. Biol. 208, 193–202.
Kucerka, N., van Oosten, B., Pan, J.J., Heberle, F.A., Harroun, T.A., Katsaras, J., 2015a. Molecular structures of fluid phosphatidylethanolamine bilayers obtained from simulation-to-experiment comparisons and experimental scattering density profiles. J. Phys. Chem. B 119, 1947–1956.
Kučerka, N., Perlmutter, J.D., Pan, J., Tristram-Nagle, S., Katsaras, J., Sachs, J.N., 2008. The effect of cholesterol on short-and long-chain monounsaturated lipid bilayers as determined by molecular dynamics simulations and X-ray scattering. Biophys. J. 95, 2792–2805.
Lee, S., Tran, A., Allsopp, M., Lim, J.B., Hénin, J., Klauda, J.B., 2014. CHARMM36 united atom chain model for lipids and surfactants. J. Phys. Chem. B 118, 547–556.
Li, Z., Venable, R.M., Rogers, L.A., Murray, D., Pastor, R.W., 2009. Molecular dynamics simulations of PIP2 and PIP3 in lipid bilayers: determination of ring orientation, and the effects of surface roughness on a Poisson-Boltzmann description. Biophys. J. 97, 155–163.
Marquardt, D., Heberle, F.A., Pan, J., Cheng, X., Pabst, G., Harroun, T.A., Kučerka, N., Katsaras, J., 2020. The structures of polyunsaturated lipid bilayers by joint refinement of neutron and X-ray scattering data. Chem. Phys. Lipids 229, 104892.
Matsuki, H., Miyazaki, E., Sakano, F., Tamai, N., Kaneshina, S., 2007. Thermotropic and barotropic phase transitions in bilayer membranes of ether-linked phospholipids with varying alkyl chain lengths. Biochim. Et. Biophys. Acta-Biomembr. 1768, 479–489.
Mcintosh, T.J., Simon, S.A., Ellington, J.C., Porter, N.A., 1984. New Structural Model for Mixed-Chain Phosphatidylcholine Bilayers. Biochem. -Us 23, 4038–4044.
McIntosh, T.J., Simon, S.A., 1986. Area per molecule and distribution of water in fully hydrated dilauroylphosphatidylethanolamine bilayers. Biochemistry 25, 4948–4952.
Nagle, J.F., 1980. Theory of the main lipid bilayer phase-transition. Annu Rev. Phys. Chem. 31, 157–195.
Nagle, J.F., 1993. Evidence for partial rotational order in gel phase dppc. Biophys. J. 64, 1110–1112.
Nagle, J.F., 2013. Introductory Lecture: basic quantities in model biomembranes. Faraday Discuss. 161, 11–29.
Nagle, J.F., 2023. Understanding the phase behavior of a protobiomembrane. Phys. Rev. E 107, 7.
Nagle, J.F., Akabori, K., Treece, B.W., Tristram-Nagle, S., 2016. Determination of mosaicity in oriented stacks of lipid bilayers. Soft Matter 12, 1884–1891.
Nagle, J.F., Cognet, P., Dupuy, F.G., Tristram-Nagle, S., 2019a. Structure of gel phase DPPC determined by X-ray diffraction. Chem. Phys. Lipids 218, 168–177.
Nagle, J.F., Jennings, N., Qin, W.H., Yan, D.N., Tristram-Nagle, S., Heinrich, F., 2023. Structure of the gel phase of diC22:1PC lipid bilayers determined by x-ray diffraction. Biophys. J. 122, 1033–1042.
Nagle, J.F., Tristram-Nagle, S., 2000. Structure of lipid bilayers. Bba-Rev. Biomembr. 1469, 159–195.

Nagle, J.F., Venable, R.M., Maroclo-Kemmerling, E., Tristram-Nagle, S., Harper, P.E., Pastor, R.W., 2019b. Revisiting volumes of lipid components in bilayers. J. Phys. Chem. B 123, 2697–2709.
Nagle, J.F., Wiener, M.C., 1989. Relations for lipid bilayers - connection of electron-density profiles to other structural quantities. Biophys. J. 55, 309–313.
Nagle, J.F., Zhang, R.T., TristramNagle, S., Sun, W.J., Petrache, H.I., Suter, R.M., 1996. X-ray structure determination of fully hydrated L(alpha) phase dipalmitoylphosphatidylcholine bilayers. Biophys. J. 70, 1419–1431.
Neale, C., K, H., Garcia, A.E., TristramNagle, S., 2015. Penetration of HIV-1 Tat47-57 into PC/PE bilayers assessed by MD simulation and X-ray scattering. Membranes 5, 473–494.
Ollila, S., Kiirikki, A., Antila, H., Bort, L., Buslaev, P., Favela, F., Ferreira, T., Fuchs, P., Garcia-Fandino, R., Gushchin, I., Kav, B., Kula, P., Kurki, M., Kuzmin, A., Madsen, J., Miettinen, M., Nencini, R., Piggot, T., Pineiro, A., Samantray, S., Suarez-Leston, F., 2023. NMRlipids Databank makes data-driven analysis of biomembrane properties accessible for all. Eur. Biophys. J. Biophy 52. S146-S146.
Ollila, O.S., Pabst, G., 2016. Atomistic resolution structure and dynamics of lipid bilayers in simulations and experiments. Biochim. Et. Biophys. Acta (BBA)-Biomembr. 1858, 2512–2528.
Pan, J.J., Cheng, X.L., Heberle, F.A., Mostofian, B., Kucerka, N., Drazba, P., Katsaras, J., 2012b. Interactions between ether phospholipids and cholesterol as determined by scattering and molecular dynamics simulations. J. Phys. Chem. B 116, 14829–14838.
Pan, J.J., Cheng, X.L., Monticelli, L., Heberle, F.A., Kucerka, N., Tieleman, D.P., Katsaras, J., 2014. The molecular structure of a phosphatidylserine bilayer determined by scattering and molecular dynamics simulations. Soft Matter 10, 3716–3725.
Pan, J.J., Heberle, F.A., Tristram-Nagle, S., Szymanski, M., Koepfinger, M., Katsaras, J., Kucerka, N., 2012a. Molecular structures of fluid phase phosphatidylglycerol bilayers as determined by small angle neutron and X-ray scattering. Biochim. Et. Biophys. Acta-Biomembr. 1818, 2135–2148.
Petrache, H.I., Tristram-Nagle, S., Gawrisch, K., Harries, D., Parsegian, V.A., Nagle, J.F., 2004. Structure and fluctuations of charged phosphatidylserine bilayers in the absence of salt. Biophys. J. 86, 1574–1586.
Poger, D., Caron, B., Mark, A.E., 2016. Validating lipid force fields against experimental data: Progress, challenges and perspectives. Biochim. Et. Biophys. Acta (BBA)-Biomembr. 1858, 1556–1565.
Rand, R.P., Parsegian, V.A., 1989. Hydration forces between phospholipid-bilayers. Biochim. Biophys. Acta 988, 351–376.
Raghunathan, M., Zubovski, Y., Venable, R.M., Pastor, R.W., Nagle, J.F., Tristram-Nagle, S., 2012. Structure and elasticity of lipid membranes with genistein and daidzein bioflavinoids using X-ray scattering and MD simulations. J. Phys. Chem. B 116, 3918–3927.
Rand, R.P., Fuller, N.L., Gruner, S.M., Parsegian, V.A., 1990. Membrane curvature, lipid segregation, and structural transitions for phospholipids under dual-solvent stress. Biochem. -Us 29, 76–87.
Ruocco, M.J., Shipley, G.G., 1982. Characterization of the sub-transition of hydrated dipalmitoylphosphatidylcholine bilayers - kinetic, hydration and structural study. Biochim. Biophys. Acta 691, 309–320.
Seelig, J., Seelig, A., 1980. Lipid conformation in model membranes and biological-membranes. Q Rev. Biophys. 13, 19–61.
Sengupta, K., Raghunathan, V.A., Katsaras, J., 2003. Structure of the ripple phase of phospholipid multibilayers. Phys. Rev. E 68.
Serrallach, E., De Haas, G., Shipley, G., 1984. Structure and thermotropic properties of mixed-chain phosphatidylcholine bilayer membranes. Biochemistry 23, 713–720.
Shekhar, P., Nanda, H., Lösche, M., Heinrich, F., 2011. Continuous distribution model for the investigation of complex molecular architectures near interfaces with scattering techniques. J. Appl. Phys. 110, 102216.
Small, D.M., 1986. The Physical Chemistry of Lipids, 4. Plenum Press, New York.
Smith, G.S., Safinya, C.R., Roux, D., Clark, N.A., 1987. X-ray study of freely suspended films of a multilamellar lipid system. Mol. Cryst. Liq. Cryst. 144, 235–255.
Smith, G.S., Sirota, E.B., Safinya, C.R., Plano, R.J., Clark, N.A., 1990. X-Ray Structural Studies of Freely Suspended Ordered Hydrated Dmpc Multimembrane Films. J. Chem. Phys. 92, 4519–4529.
Sun, W.J., Suter, R.M., Knewtson, M.A., Worthington, C.R., Tristram-Nagle, S., Zhang, R., Nagle, J.F., 1994. Order and disorder in fully hydrated unoriented bilayers of gel phase dipalmitoylphosphatidylcholine. Phys. Rev. E 49, 4665–4676.
Sun, W.J., TristramNagle, S., Suter, R.M., Nagle, J.F., 1996a. Structure of gel phase saturated lecithin bilayers: temperature and chain length dependence. Biophys. J. 71, 885–891.
Sun, W.J., TristramNagle, S., Suter, R.M., Nagle, J.F., 1996b. Structure of the ripple phase in lecithin bilayers. P Natl. Acad. Sci. 93, 7008–7012.
Tardieu, A., Luzzati, V., Reman, F.C., 1973. Structure anD Polymorphism of Hydrocarbon Chains of Lipids - Study of Lecithin-water Phases. J. Mol. Biol. 75, 711.
Tjornhammar, R., Edholm, O., 2014. Reparameterized united atom model for molecular dynamics simulations of gel and fluid phosphatidylcholine bilayers. J. Chem. Theory Comput. 10, 5706–5715.
Tristram-Nagle, S., Isaacson, Y., Lyatskaya, Y., Liu, Y.F., Brummond, K., Katsaras, J., Nagle, J.F., 1999. Polymorphism in myristoylpalmitoylphosphatidylcholine. Chem. Phys. Lipids 100, 101–113.
Tristram-Nagle, S., Liu, Y.F., Legleiter, J., Nagle, J.F., 2002. Structure of gel phase DMPC determined by X-ray diffraction. Biophys. J. 83, 3324–3335.
Tristram-Nagle, S., Zhang, R., Suter, R.M., Worthington, C.R., Sun, W.J., Nagle, J.F., 1993. Measurement of chain tilt angle in fully hydrated bilayers of gel phase lecithins. Biophys. J. 64, 1097–1109.
Tu, K., Tobias, D.J., Klein, M.L., 1995. Molecular-dynamics simulations of phospholipid-bilayers. Abstr. Pap. Am. Chem. S 210, 151-PHYS.
Uhrikova, D., Rybar, P., Hianik, T., Balgavy, P., 2007. Component volumes of unsaturated phosphatidylcholines in fluid bilayers: a densitometric study. Chem. Phys. Lipids 145, 97–105.
Venable, R.M., Brooks, B.R., Pastor, R.W., 2000. Molecular dynamics simulations of gel (L-beta I) phase lipid bilayers in constant pressure and constant surface area ensembles. J. Chem. Phys. 112, 4822–4832.
Wack, D.C., Webb, W.W., 1989. Synchrotron X-ray study of the modulated lamellar phase P-Beta' in the lecithin-water system. Phys. Rev. A 40, 2712–2730.
Wiener, M.C., Suter, R.M., Nagle, J.F., 1989. Structure of the fully hydrated gel phase of dipalmitoylphosphatidylcholine. Biophys. J. 55, 315–325.
Wiener, M.C., Tristramnagle, S., Wilkinson, D.A., Campbell, L.E., Nagle, J.F., 1988. Specific volumes of lipids in fully hydrated bilayer dispersions. Biochim Biophys. Acta 938, 135–142.
Wiener, M.C., White, S.H., 1991. Fluid bilayer structure determination by the combined use of x-ray and neutron diffraction. I. Fluid bilayer models and the limits of resolution. Biophys. J. 59, 162–173.
Yu, Y.L., Krämer, A., Venable, R.M., Brooks, B.R., Klauda, J.B., Pastor, R.W., 2021. CHARMM36 lipid force field with explicit treatment of long-range dispersion: parametrization and validation for phosphatidylethanolamine, phosphatidylglycerol, and ether lipids. J. Chem. Theory Comput. 17, 1581–1595.
Yu, Y., Venable, R.M., Thirman, J., Chatterjee, P., Kumar, A., Pastor, R.W., Roux, B., MacKerell Jr, A.D., Klauda, J.B., 2023. Drude polarizable lipid force field with explicit treatment of long-range dispersion: parametrization and validation for saturated and monounsaturated zwitterionic lipids. J. Chem. Theory Comput. 19, 2590–2605.
Zaccai, G., Buldt, G., Seelig, A., Seelig, J., 1979. Neutron-diffraction studies on phosphatidylcholine model membranes.2. chain conformation and segmental disorder. J. Mol. Biol. 134, 693–706.